



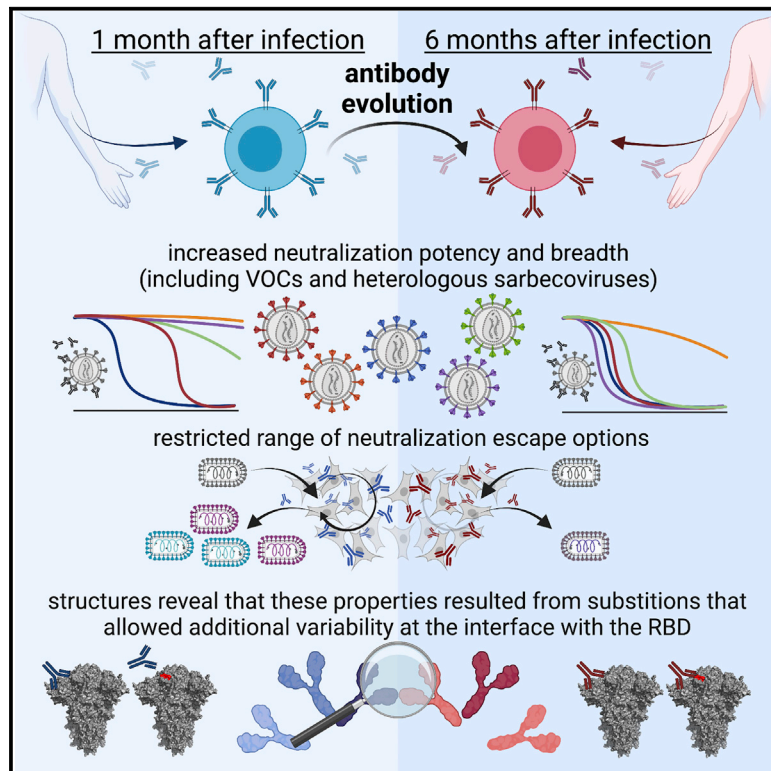
Since January 2020 Elsevier has created a COVID-19 resource centre with free information in English and Mandarin on the novel coronavirus COVID-19. The COVID-19 resource centre is hosted on Elsevier Connect, the company's public news and information website.

Elsevier hereby grants permission to make all its COVID-19-related research that is available on the COVID-19 resource centre - including this research content - immediately available in PubMed Central and other publicly funded repositories, such as the WHO COVID database with rights for unrestricted research re-use and analyses in any form or by any means with acknowledgement of the original source. These permissions are granted for free by Elsevier for as long as the COVID-19 resource centre remains active.

# Immunity

## Affinity maturation of SARS-CoV-2 neutralizing antibodies confers potency, breadth, and resilience to viral escape mutations

### Graphical abstract



### Highlights

- Maturation over months increases potency of SARS-CoV-2 neutralizing antibodies
- Antibody maturation restricts options for viral escape
- Maturation of some antibodies enables neutralization of additional sarbecoviruses
- Antibody-spike structures reveal changes that improve potency and breadth

### Authors

Frauke Muecksch, Yiska Weisblum, Christopher O. Barnes, ..., Pamela J. Bjorkman, Theodora Hatziioannou, Paul D. Bieniasz

### Correspondence

nussen@mail.rockefeller.edu (M.C.N.), bjorkman@caltech.edu (P.J.B.), thatzio@rockefeller.edu (T.H.), pbieniasz@rockefeller.edu (P.D.B.)

### In brief

SARS-CoV-2 RBD-binding antibodies accumulate mutations over months of convalescence, but how maturation affects antibody properties is unclear. Muecksch et al. analyze 6 groups of clonally related neutralizing antibodies from convalescent donors and reveal that antibody maturation increases affinity, potency, and breadth, and restricts viral escape options. They also identify the structural basis for these improved antibody properties during maturation.



## Article

# Affinity maturation of SARS-CoV-2 neutralizing antibodies confers potency, breadth, and resilience to viral escape mutations

Frauke Muecksch,<sup>1,6</sup> Yiska Weisblum,<sup>1,6</sup> Christopher O. Barnes,<sup>2,6</sup> Fabian Schmidt,<sup>1,6</sup> Dennis Schaefer-Babajew,<sup>3</sup> Zijun Wang,<sup>3</sup> Julio C. C. Lorenzi,<sup>3</sup> Andrew I. Flyak,<sup>2</sup> Andrew T. DeLaitch,<sup>2</sup> Kathryn E. Huey-Tubman,<sup>2</sup> Shurong Hou,<sup>4</sup> Celia A. Schiffer,<sup>4</sup> Christian Gaebler,<sup>3</sup> Justin Da Silva,<sup>1</sup> Daniel Poston,<sup>1</sup> Shlomo Finkin,<sup>3</sup> Alice Cho,<sup>3</sup> Melissa Cipolla,<sup>3</sup> Thiago Y. Oliveira,<sup>3</sup> Katrina G. Millard,<sup>3</sup> Victor Ramos,<sup>3</sup> Anna Gazumyan,<sup>3</sup> Magdalena Rutkowska,<sup>1</sup> Marina Caskey,<sup>3</sup> Michel C. Nussenzweig,<sup>3,5,\*</sup> Pamela J. Bjorkman,<sup>2,\*</sup> Theodora Hatziioannou,<sup>1,\*</sup> and Paul D. Bieniasz<sup>1,5,7,\*</sup>

<sup>1</sup>Laboratory of Retrovirology, The Rockefeller University, New York, NY 10065, USA

<sup>2</sup>Division of Biology and Biological Engineering, California Institute of Technology, Pasadena, CA 91125, USA

<sup>3</sup>Laboratory of Molecular Immunology, The Rockefeller University, New York, NY 10065, USA

<sup>4</sup>Department of Biochemistry and Molecular Pharmacology, University of Massachusetts Medical School, Worcester, MA 01655, USA

<sup>5</sup>Howard Hughes Medical Institute

<sup>6</sup>These authors contributed equally

<sup>7</sup>Lead contact

\*Correspondence: [nussen@mail.rockefeller.edu](mailto:nussen@mail.rockefeller.edu) (M.C.N.), [bjorkman@caltech.edu](mailto:bjorkman@caltech.edu) (P.J.B.), [thatziio@rockefeller.edu](mailto:thatziio@rockefeller.edu) (T.H.), [pbieniasz@rockefeller.edu](mailto:pbieniasz@rockefeller.edu) (P.D.B.)

<https://doi.org/10.1016/j.immuni.2021.07.008>

## SUMMARY

Antibodies elicited by infection accumulate somatic mutations in germinal centers that can increase affinity for cognate antigens. We analyzed 6 independent groups of clonally related severe acute respiratory syndrome-coronavirus-2 (SARS-CoV-2) Spike receptor-binding domain (RBD)-specific antibodies from 5 individuals shortly after infection and later in convalescence to determine the impact of maturation over months. In addition to increased affinity and neutralization potency, antibody evolution changed the mutational pathways for the acquisition of viral resistance and restricted neutralization escape options. For some antibodies, maturation imposed a requirement for multiple substitutions to enable escape. For certain antibodies, affinity maturation enabled the neutralization of circulating SARS-CoV-2 variants of concern and heterologous sarbecoviruses. Antibody-antigen structures revealed that these properties resulted from substitutions that allowed additional variability at the interface with the RBD. These findings suggest that increasing antibody diversity through prolonged or repeated antigen exposure may improve protection against diversifying SARS-CoV-2 populations, and perhaps against other pandemic threat coronaviruses.

## INTRODUCTION

Neutralizing antibodies elicited by infection or vaccination are a central component of immunity to subsequent challenge by viruses (Plotkin, 2010) and can also confer passive immunity in prophylactic or therapeutic settings. In the case of severe acute respiratory syndrome-coronavirus-2 (SARS-CoV-2), an understanding of how viral variants evade antibodies and how affinity maturation could generate antibodies that maintain activity against viral variants is important to guide vaccination and treatment strategies.

The receptor-binding domains (RBDs) of the SARS-CoV-2 Spike trimer are key neutralization targets, and potent RBD-specific antibodies have been isolated from many convalescent donors (Brouwer et al., 2020; Cao et al., 2020; Chen et al., 2020; Chi et al., 2020; Hansen et al., 2020; Ju et al., 2020; Kreer et al., 2020; Robbiani et al., 2020; Rogers et al.,

2020; Seydoux et al., 2020; Shi et al., 2020; Wec et al., 2020; Wu et al., 2020b; Zost et al., 2020). Such antibodies are used for the treatment of SARS-CoV-2 infection (Chen et al., 2021; Weinreich et al., 2021). Typically, RBD-specific neutralizing antibodies isolated during early convalescence have low levels of somatic hypermutation, and nearly identical antibodies derived from specific rearranged antibody genes (e.g., VH3-53/VH3-63) (Barnes et al., 2020b; Robbiani et al., 2020; Yuan et al., 2020) are found in distinct convalescent or vaccinated individuals (Wang et al., 2021b). Consistent with these findings, high titer neutralizing sera are generated following the administration of at least some SARS-CoV-2 vaccines (Sahin et al., 2020; Widge et al., 2021). Conversely, SARS-CoV-2 infection may sometimes fail to induce sufficient B cell stimulation and expansion to generate high neutralizing antibody titers. Neutralizing titers are low in some convalescent individuals, including those from whom commonly



elicited potent antibodies can be cloned (Luchsinger et al., 2020; Robbiani et al., 2020; Wu et al., 2020a).

The RBD exhibits flexibility and binds the angiotensin-converting enzyme 2 (ACE2) receptor only in an “up” conformation, not in the “down” RBD conformation of the closed, prefusion trimer (Walls et al., 2020; Wrapp et al., 2020). Structural studies have allowed the designation of distinct RBD-binding antibody structural classes (Barnes et al., 2020b). Class 1 antibodies are derived from *VH3-53* or *VH3-63* gene segments, include short CDRH3s, and recognize the ACE2 binding site on RBDs in an up conformation (Barnes et al., 2020a, 2020b; Hurlburt et al., 2020; Shi et al., 2020; Wu et al., 2020c; Yuan et al., 2020). Class 2 antibodies are derived from a variety of VH gene segments, also target the ACE2 binding site, but can bind to RBDs in either an up or a down conformation. Some class 2 antibodies (e.g., C144, S2M11) (Barnes et al., 2020a; Tortorici et al., 2020) bridge adjacent down RBDs to lock the Spike trimer into a closed prefusion conformation. Class 3 antibodies, which can recognize up or down RBDs, do not target the ACE2 binding site (Barnes et al., 2020a).

Despite the fact that cloned RBD-specific antibodies can select resistance mutations, such as E484K, in cell culture (Baum et al., 2020; Weisblum et al., 2020), until recently, little evidence had emerged that antibodies have imposed selective pressure on circulating SARS-CoV-2 populations. Nevertheless, variability and decay of convalescent neutralizing titers (Gaebler et al., 2021; Luchsinger et al., 2020; Muecksch et al., 2021; Robbiani et al., 2020; Seow et al., 2020) suggests that reinfection by SARS-CoV-2 may occur with some frequency. Recent reports have documented reinfection or rapidly increasing case numbers associated with SARS-CoV-2 variants with resistance to commonly elicited antibodies (Fujino et al., 2021; Tegally et al., 2020; Volz et al., 2021; Wang et al., 2021b; West et al., 2021; Wibmer et al., 2021).

The majority of SARS-CoV-2 antibodies that have been studied in detail were cloned from individuals early in convalescence and have relatively low numbers of somatic mutations. However, recent work has shown that antibodies evolve in convalescent patients, accumulating somatic mutations that can affect function (Gaebler et al., 2021; Sakharkar et al., 2021; Sokal et al., 2021). Here, we present a detailed functional and structural characterization of several groups of clonally related antibodies recovered from the same 5 individuals shortly after infection and then later in convalescence. We show that somatic mutations acquired in the months after infection endow some SARS-CoV-2 RBD-specific antibodies with greater neutralization potency and breadth. We further show that the acquisition of somatic mutations enables some antibodies to maintain activity in instances in which viral mutations would otherwise enable escape from neutralization.

## RESULTS

### SARS-CoV-2 RBD-specific antibody sequences evolve during convalescence

We studied RBD-specific antibodies selected from a set of 1,072 that were cloned from a cohort of convalescent individuals who were studied at a mean of 1.3 and 6.2 months after PCR diagnosis of mild to moderately severe coronavirus disease 2019 (COVID-19) (Gaebler et al., 2021; Robbiani et al., 2020). Antibody

sequences found at 6.2 months were more divergent than sequences found at 1.3 months from their unmutated common ancestors, illustrating continued antibody evolution during convalescence (Gaebler et al., 2021). To determine the functional consequences of maturation of clonally related antibodies during SARS-CoV-2 convalescence, we analyzed 6 representative antibody groups from 5 different participants (Figure S1A; Table S1), with members of each antibody group isolated at 1.3 and 6.2 months (Gaebler et al., 2021; Robbiani et al., 2020). Selection of the antibodies were based on the approximate frequency of antibody RBD-binding classes found in our convalescent cohort. Class 2 is the predominant antibody class found in convalescent individuals, but class 1 and class 3 antibodies are also encountered frequently (Gaebler et al., 2021; Robbiani et al., 2020). We measured antibody affinity, using Bi-layer interferometry (BLI) and neutralization potency against a panel of SARS-CoV-2 pseudotypes with substitutions that can confer resistance to neutralization by human antibodies (Weisblum et al., 2020). In addition, to determine the ability of the SARS-CoV-2 Spike to acquire mutations conferring resistance, we used replication-competent chimeric vesicular stomatitis virus (VSV) derivatives (rVSV/SARS-CoV-2<sub>1D7/2E1</sub>) (Schmidt et al., 2020; Weisblum et al., 2020) to select escape variants for each of the antibodies.

### Maturation increases the potency and resilience of class 2 SARS-CoV-2 neutralizing antibodies

Class 2 anti-RBD antibodies are commonly elicited and recognize an epitope that includes E484 (Barnes et al., 2020a), which is mutated in certain circulating SARS-CoV-2 “variants of concern” (VOC) (Fujino et al., 2021; West et al., 2021; Wibmer et al., 2021). We examined members of 3 class 2 antibody groups. One group of class 2, *VH3-53/VL2-14*-encoded antibodies included C144, a potent neutralizing antibody (half-maximal inhibitory concentration [IC<sub>50</sub>] <10 ng/mL) isolated at 1.3 months of convalescence (Robbiani et al., 2020), which is in clinical development for therapy/prophylaxis. Two clonally related antibodies subsequently isolated from the C144 donor at 6.2 months included C051, which was marginally less potent (IC<sub>50</sub> ~25 ng/mL), and C052, which had similar potency to C144 (Gaebler et al., 2021). C051 and C052 had ~4-fold greater somatic hypermutation (SHM) frequency compared to C144 (Table S1).

SARS-CoV-2 pseudotype neutralization assay revealed that several RBD substitutions at positions L455, F456, E484, F490, Q493, and S494, which conferred C144 resistance, had no effect on C051 and C052 sensitivity (Figures 1A and 1B). Some, but not all, naturally occurring E484 substitutions that conferred C144 resistance also conferred resistance to C051 and/or C052. Consistent with this finding, C051 and C052 had increased affinity for Q493R mutant RBD compared to C144, but remained unable to bind the E484K RBD (Figures 1C and S1B). Selection for C144 resistance mutations using rVSV/SARS-CoV-2 yielded multiple substitutions at 2 positions; E484K/A/G and Q493R/K (Figure 1D), and plaque purification from selected virus populations yielded isolates with E484K or Q493R substitutions that confer C144 resistance (Weisblum et al., 2020). Conversely, rVSV/SARS-CoV-2 replication in the presence of C051 and C052 led to the dominance of the E484K mutant only, and rVSV/SARS-CoV-2 isolates bearing E484K substitutions were

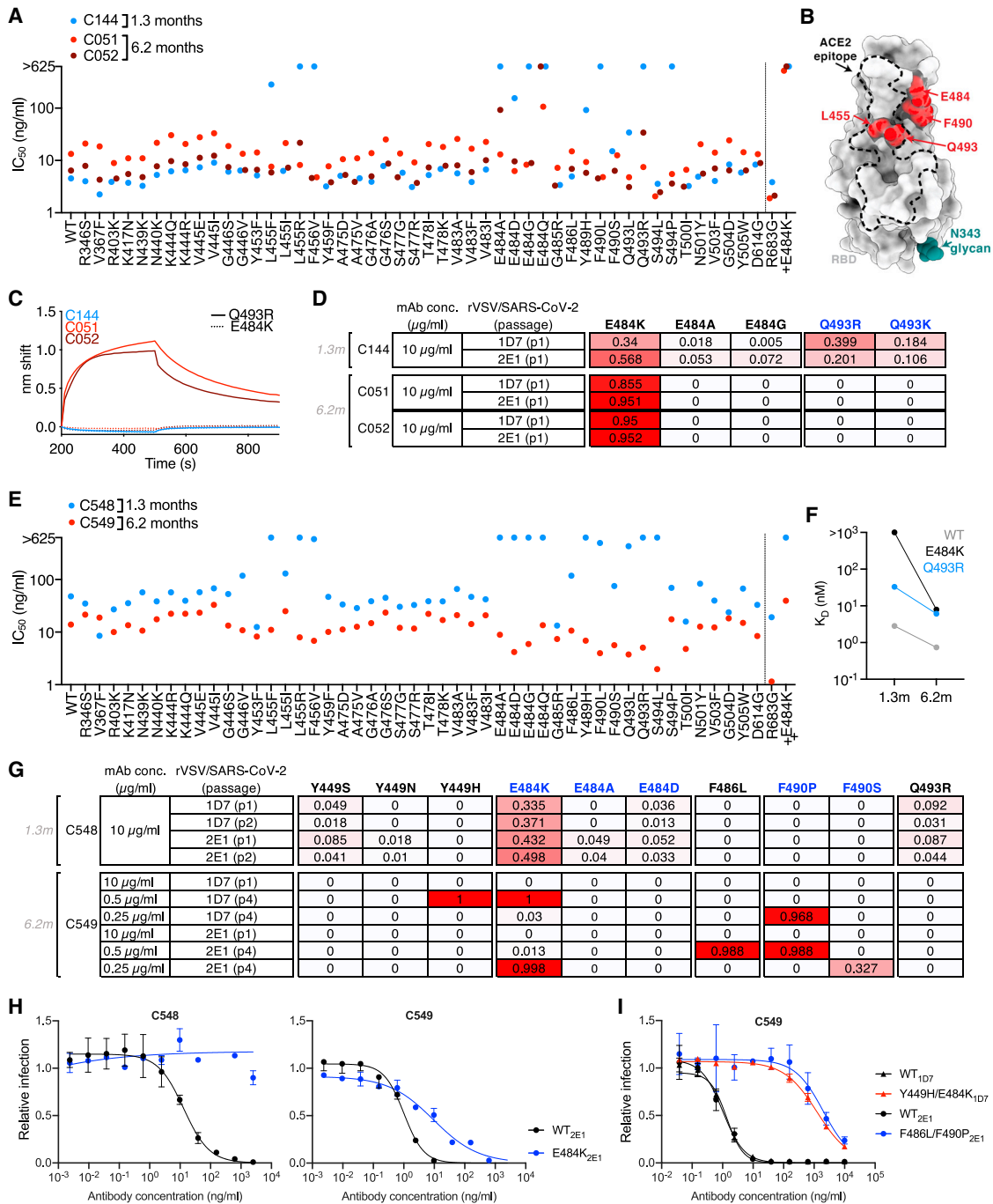


**Figure 1. Somatic mutation of class 2 antibodies affects potency and viral escape potential**

(A) Neutralization potency ( $IC_{50}$ ) of C144, C051, and C052 measured using HIV-1-based SARS-CoV-2 variant pseudotypes and HT1080/ACE2cl.14 cells. The E484K substitution was constructed in an R683G (furin cleavage site mutant) background to increase infectivity. Mean of 2 independent experiments.

(B) RBD structure indicating positions of substitutions that affect sensitivity to neutralization by class 2 and C144/C051/C052, C143/C164/C055, and C548/549 antibodies.

(C) BLI affinity measurements for indicated antibodies against Q493R and E484K RBD, shown as continuous and dotted lines, respectively.

(D) Decimal fraction (color gradient; white = 0, red = 1) of Illumina sequence reads encoding the indicated RBD substitutions following rVSV/SARS-CoV-2 replication (1D7 and 2E1 virus isolates) in the presence of the indicated amounts of antibodies for the indicated number of passages.

(E) As in (A) for antibodies C548 and C549.

(F) BLI affinity measurements for C548 (1.3 month) and C549 (6.2 month) for the indicated RBD proteins.

(legend continued on next page)

resistant to C051 and C052 (Figures 1D and S2A). Thus, affinity maturation of this clonally related family of potentially neutralizing antibodies enabled the retention of activity against a subset of naturally occurring potential escape variants. Nevertheless, the E484K substitution conferred resistance to each of the antibodies in this commonly elicited class (Figures 1A, 1B, and S2A).

A second clonally related group of antibodies, encoded by *VH3-66/VL2-33*, included C143 and C164, isolated at 1.3 months, and C055, isolated at 6.2 months, were from the same individual as the C144 group (Gaebler et al., 2021; Robbiani et al., 2020; Figure S1A). C143 and C164 had weak neutralizing activity ( $IC_{50}$  values  $\sim 300 \rightarrow 625$  ng/mL) against the HIV-1 pseudotype panel (Figure S2B). Conversely, C055 potentially neutralized the majority of SARS-CoV-2 Spike variant pseudotypes ( $IC_{50}$  values of  $\sim 10$  ng/mL) (Figure S2B). C143 and C164 had quite high SHM frequencies relative to other 1.3-month antibodies, but this was further increased in C055 (Table S1). While the increased potency of C055 was not fully reflected by changes in the affinity for the wild-type (WT) RBD, C055 exhibited clearly increased affinity for the E484K mutant RBD (Figure S1B). Naturally occurring Spike substitutions (at positions A475, T478, E484, G485, and F486) reduced C055 potency (Figure S2B), indicating a target epitope close to that of the C144/C051/C052 antibody group. Despite their modest potency, rVSV/SARS-CoV-2 replication with C143 or C164 led to the enrichment of T478K/R mutations, and a plaque-purified T478R mutant isolate exhibited near-complete resistance to C143 and C164, while an E484K mutant exhibited partial resistance (Figures S2C and S2D). Conversely rVSV/SARS-CoV-2 selection with C055 yielded G485S/D and F486V/S mutations, and isolates with G485S, F486S, or F486V substitutions exhibited nearly complete resistance to C055 (Figures S2C and S2E). Overall, maturation of this clonally related class 2 antibody group yielded both greater potency and a change in the selected Spike substitutions that yielded neutralization escape (Figure S2C).

A third group of class 2 antibodies, encoded by *VH1-69/VL9-49*, included C548, isolated at 1.3 months, and C549, isolated at 6.2 months (Gaebler et al., 2021; Robbiani et al., 2020; Figure S1A). Notably, C548 had a near germline sequence with only 1 nucleotide mismatch in the light chain, while C549 acquired 13 and 8 nucleotide mismatches in the heavy and light chains, respectively (Table S1). C548 was somewhat less potent ( $IC_{50} \sim 50$  ng/mL) than C549 ( $IC_{50} \sim 15$  ng/mL) and had a commensurately lower binding affinity for WT RBD (Figures 1E, 1F, and S1B). Similar to C144, naturally occurring substitutions at positions L455, F456, E484, Y489, S494, Q493, and S494 caused a near-complete loss of C548 potency (Figure 1E). However, C549 potency was unaffected or only marginally affected by most of these mutations (Figure 1E), properties that were reflected in its increased binding affinity for Q493R and E484K RBD (Figure 1F). E484K conferred partial ( $\sim 50$ - to 100-fold) resistance to C549 (Figure 1G) and reduced binding affinity ( $\sim 10$ -fold) compared to WT. Selection experiments with C548 and rVSV/SARS-CoV-2 led to rapid enrichment of resistant mu-

tants (E484K and Q493R; Figures 1G and 1H), consistent with the finding that E484K or Q493R substitutions conferred C548 resistance in the HIV-1 pseudotype assay (Figures 1E and S3A). In contrast, initial attempts to select C549-resistant rVSV/SARS-CoV-2 mutants failed (Figure 1G). However, by reducing the selecting concentration of C549 and sequential passaging with antibody 4 times, we obtained rVSV/SARS-CoV-2 populations in which Y449H, E484K, F486L, and F490P/S mutations were enriched (Figure 1G). Notably, these selected populations yielded only isolates that encoded 2 RBD substitutions; one Y449H/E484K and the other F486L/F490P. These viruses exhibited greater (1,000-fold) C549 resistance than the E484K single mutant (Figures 1I, S3A, and S3B). Because individual substitutions at Y449, E484, F486, and F490 caused only partial or no C549 resistance (Figures 1E, 1I, and S3), these data suggest that at least 2 substitutions are required to confer a large diminution in C549 potency. Thus, for the C548/C549 antibody pair, affinity maturation appeared to heighten the genetic barrier for the acquisition of antibody resistance.

#### Affinity maturation confers potency and resilience to escape in a class 1 antibody clone

A fourth group of clonally related antibodies, encoded by *VH3-53/VK3-20* genes, also exhibited a large disparity in activity and breadth when 1.3- and 6.2-month clonal relatives were compared. Specifically, C098, isolated at 1.3 months, displayed minimal activity ( $IC_{50} > 1,000$  ng/mL) against most SARS-CoV-2 pseudotypes while a clonal relative isolated at 6.2 months, C099, had  $IC_{50}$  values ranging from  $\sim 15$  to 48 ng/mL for all of the variants except L455R, for which the  $IC_{50}$  was increased to 123 ng/mL (Figures 2A and 2B). C099 also exhibited greatly increased binding affinity for WT RBD when compared to C098 (Figure S1B). In rVSV/SARS-CoV-2 selection experiments, the low potency of C098 was reflected in the modest enrichment of mutations. Nevertheless, there was some enrichment of N460 substitutions (Figures 2B and 2C), and after 2 passages, the rVSV/SARS-CoV-2 (N460Y) mutant was isolated that displayed nearly complete C098 resistance (Figure 2D).

Initial attempts to isolate C099-resistant rVSV/SARS-CoV-2 mutants failed. However, passaging rVSV/SARS-CoV-2 4 times in the presence of reduced concentrations of C099 yielded populations enriched most prominently in D420Y, Y453H, and L455R substitutions (Figures 2B and 2C). Plaque purification yielded D420Y, N460Y, or L455R single mutants with partial ( $\leq 10$ -fold increase in  $IC_{50}$ ) C099 resistance (Figures 2B, 2E, and 2F) as well as D420Y/N460H and L455R/Y453H double mutants with a higher degree of C099 neutralization resistance ( $\sim 100$ -fold increase in  $IC_{50}$ ; Figures 2E and 2F). Analysis of HIV-1 pseudotypes with these mutations confirmed that D420Y, N460H, L455R, and Y453H alone each abolished the weak C098 neutralization activity but conferred no or partial C099 resistance (Figures S4A and S4B). However, the D420Y/N460H or L455R/Y453H combinations conferred greater C099 resistance (Figure S4B). Overall, affinity maturation of C098/99 conferred both greatly increased potency

(G) As in (D) for antibodies C548 and C549. Reduced antibody concentrations were required for C549 escape.

(H and I) C548 (H) and C549 (I) neutralization of rVSV/SARS-CoV-2 1D7, 2E1, or plaque-purified mutants thereof isolated following antibody selection. Infected (% GFP<sup>+</sup>) cells relative to no antibody controls; mean and range of 2 independent experiments plotted. See also Figures S2 and S3.

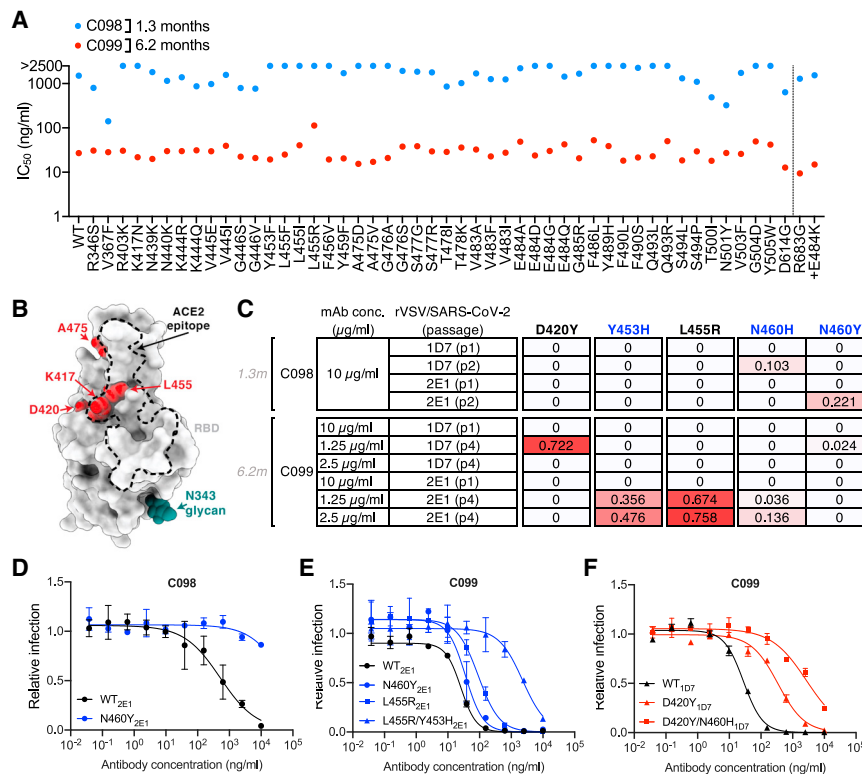


**Figure 2. Somatic mutation in a class 1 antibody confers potency and resilience to viral escape**

(A) Neutralization potency (IC<sub>50</sub>) of C098 and C099 measured using HIV-1-based SARS-CoV-2 variant pseudotypes and HT1080/ACE2cl.14 cells. The E484K substitution was constructed in an R683G (furin cleavage site mutant) background to increase infectivity. Mean of 2 independent experiments.

(B) RBD structure indicating positions of substitutions that affect sensitivity to neutralization by class 1 and C098 and C099 antibodies.

(C) Decimal fraction (color gradient; white = 0, red = 1) of Illumina sequence reads encoding the indicated RBD substitutions following rVSV/SARS-CoV-2 replication (1D7 and 2E1 virus isolates) in the presence of the indicated amounts of antibodies for the indicated number of passages.

(D–F) C098 (D) and C099 (E and F) neutralization of rVSV/SARS-CoV-2 1D7, 2E1 or plaque purified mutants thereof, isolated following antibody selection. Infected (%GFP<sup>+</sup>) cells relative to no antibody controls; mean and range of 2 independent experiments plotted.

See also Figure S4.

and appeared to impose a requirement for  $\geq 2$  mutations for large reductions in antibody-neutralizing activity.

### Class 3 antibody maturation confers potency and activity against 1.3-month antibody-resistant mutants

We next analyzed 2 pairs of class 3 antibodies, which do not directly compete for ACE2 binding to the SARS-CoV-2 RBD (Barnes et al., 2020a; Weisblum et al., 2020), yet exhibit potent neutralizing activity. Some antibodies in this class, while having very low IC<sub>50</sub> values, also exhibit incomplete neutralization in pseudotype assays—in other words, a “non-neutralizable” fraction exists for class 3 antibodies.

The VH4-4/VL2-14 encoded C132 antibody (Figure S1A), isolated at 1.3 months, had low numbers of somatic mutations (Table S1) and weak neutralizing activity against the Spike variants in the HIV-1 pseudotype assay (Figure 3A). Conversely, its 6.2-month clonal derivative, C512, had a higher degree of SHM (Table S1) displayed potency in neutralization assays (IC<sub>50</sub> ~100 ng/mL; Figure 3A) and had increased affinity for both WT and R346S mutant RBD proteins (Figure 3B). Substitutions at R346, K444, or G446 each conferred C512 resistance (Figures 3A and 3C). Despite its poor potency, rVSV/SARS-2/EGFP replication with C132 generated viral populations enriched for R346 substitutions and a plaque-purified rVSV/SARS-2/EGFP (R346K) mutant that was resistant to the weak activity of C132 (Figures 3C–3E). In contrast, and despite the fact that R346, K444, and G446 substitutions conferred resistance in the HIV-1 assay, C512 selected resistant rVSV/SARS-2/EGFP variants with K444 substitutions only (Figures 3D and 3E). Thus, maturation of the C132/C512 antibody yielded a marked increase in potency and a concurrent change in the selected resistance mutations.

For a second clonally related pair of class 3 antibodies, encoded by VH5-51/VL1-40 (Figure S1A; Table S1), the antibody isolated at 1.3 months (C032) was only ~2-fold less potent than a derivative isolated at 6.2 months (C080). However, binding affinity for WT, as well as R346S and N440K mutant RBD, was markedly increased in C080 compared to C032 and, notably, mutations at positions R346, N439, N440, K444, V445, and G446 conferred resistance to C032, but not to C080 (Figures 3F and 3G). Like some other class 3 antibodies, C032 and C080 exhibited incomplete neutralization, complicating the selection of rVSV/SARS-CoV-2-resistant variants (Figure 3H). Nevertheless, rVSV/SARS-CoV-2 selection with C032 enriched N440 and L441 substitutions, both of which conferred C032 resistance (Figure 3I). Under identical rVSV/SARS-CoV-2 selection conditions, no mutations were enriched in the presence of C080. Therefore, a key property acquired by the affinity matured antibody, C080, was retention of activity against viral mutants that escaped neutralization by its C032 progenitor.

### Affinity matured antibodies exhibit activity against SARS-CoV-2 VOC

Selection for rVSV/SARS-CoV-2 resistance to class 1, 2, and 3 antibodies in cell culture has repeatedly identified K417, E484, and N501 substitutions, with E484K giving the most pervasive effects against polyclonal plasma (Baum et al., 2020; Greaney et al., 2021; Liu et al., 2021; Wang et al., 2021b; Weisblum et al., 2020). We compared the ability of the antibodies studied herein to neutralize pseudotypes with a E484K substitution alone, or in combination with K417N and N501Y substitutions that naturally occur in the VOC (B.1.351) that exhibits the greatest degree of neutralization resistance (Fujino et al., 2021; Wibmer et al., 2021), or in

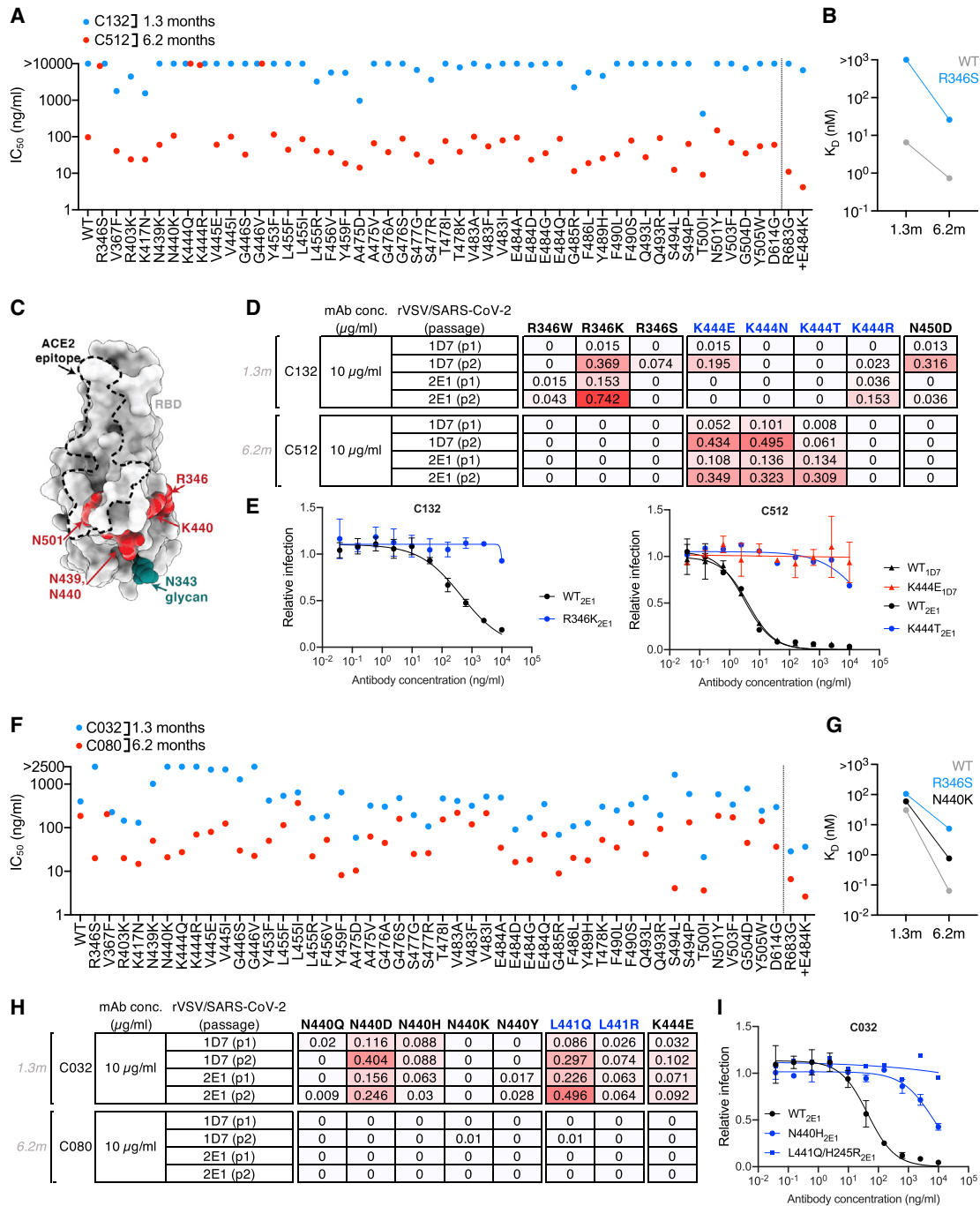


**Figure 3. Class 3 antibody maturation improves potency and reduces opportunities for viral escape**

(A) Neutralization potency ( $IC_{50}$ ) of C132 and C512 measured using HIV-1-based SARS-CoV-2 variant pseudotypes and HT1080/ACE2cl.14 cells. The E484K substitution was constructed in an R683G (furin cleavage site mutant) background to increase infectivity. Mean of 2 independent experiments.

(B) BLI affinity measurements for C132 (1.3 month) and C512 (6.2 month) for the indicated RBD proteins.

(C) RBD structure indicating positions of substitutions that affect sensitivity to neutralization by class 3 and C132/C512 and C032/C080 antibodies.

(D) Decimal fraction (color gradient; white = 0, red = 1) of Illumina sequence reads encoding the indicated RBD substitutions following rVSV/SARS-CoV-2 replication (1D7 and 2E1 virus isolates) in the presence of the indicated amounts of antibodies for the indicated number of passages.

(E) C132 and C512 neutralization of rVSV/SARS-CoV-2 1D7, 2E1, or plaque-purified mutants thereof, isolated following antibody selection. Infected (%GFP<sup>+</sup>) cells relative to no antibody controls; mean and range of 2 independent experiments plotted.

(F) As in (A) for C032 and C080.

(G) BLI affinity measurements for C032 (1.3 month) and C080 (6.2 month) for indicated RBD proteins.

(H) As in (D) for C032 and C080.

(I) As in (E) for C032.

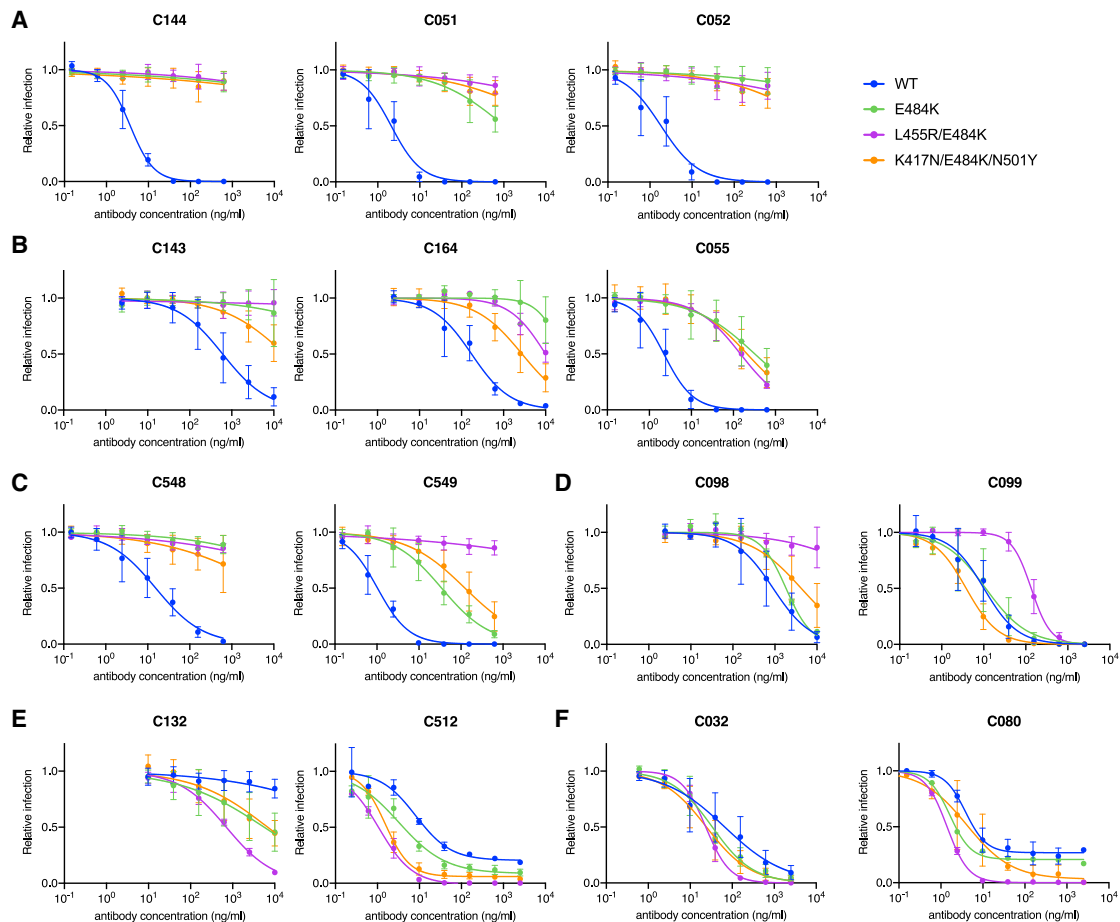


**Figure 4. E484K, K417N, N501Y, and L455R substitutions have distinct effects on matured class 1, 2, and 3 antibody sensitivity**  
Neutralization of HIV-1-based SARS-CoV-2 variant pseudotypes by C144/C051/C052 (A), C143/C164/C055 (B), C548/C549 (C), C098/C099 (D), C132/C512 (E), and C032/C080 (F) antibodies. Each of these variants was constructed in an R683G (furin cleavage site mutant) background to increase infectivity. Mean and standard deviation of 2 independent experiments.

combination with L455R, a mutation that reduced neutralization by multiple class 1 and class 2 antibodies (Figures 1 and 2). The activities of all class 2 antibodies were diminished by the E484K substitution and the K417N/E484K/N501Y combination (Figures 4A–4C). Nevertheless, while none of the antibodies in the C144/C051/C052 group show detectable affinity for and activity against E484K mutant (Figures 4A and S1B), the 6.2-month class 2 antibodies C055 and C549 exhibited increased affinity for and activity against E484K compared to their 1.3-month clonal relatives (Figures 4B, 4C, and S1B). In the case of C549, activity and affinity were modestly reduced further by the K417N/E484K/N501Y combination compared to E484K alone and abolished by the L455R/E484K combination (Figures 4C and S1B), consistent with the notion that 2 substitutions were required to confer maximal C549 escape (Figures 2E, 2F, and S3).

The C098/C099 class 1 antibodies were unaffected by the E484K mutation or the K417N/E484K/N501Y combination (Figure 4D). The partial loss of potency against the L455R/E484K combination was consistent with that seen for the L455R single mutant (Figure S4B). As expected, K417/E484K/N501Y and L455R/E484K mutations did not confer resistance to the class

3 antibodies (Figures 4E and 4F). In fact, unexpectedly, these mutations sensitized the pseudotypes to some class 3 antibodies. Thus, the E484K substitution generally undermined the activity of class 2 antibodies, but RBD substitutions found in the B.1.351 VOC did not affect the activity of the matured class 1 and class 3 antibodies tested herein.

### Maturation of antibodies elicited by SARS-CoV-2 can generate activity against additional sarbecoviruses

We next determined whether any of the antibodies could neutralize more divergent sarbecoviruses. SARS-CoV-2 is closely related to the horseshoe bat (*Rinolophus affinis*) coronavirus bCoV-RaTG13 (97.4% amino acid identity in Spike) (Zhou et al., 2020), but the SARS-CoV-2 RBD and within it the receptor binding motif (RBM) diverges from bCoV-RaTG13 (89.3% RBD and 76.4% RBM identity) and is more closely related (97.4% RBD and 98.6% RBM identity) to a pangolin (*Manis javanica*) coronavirus from Guangdong, China (pCoV-GD). The RBD of a second pangolin coronavirus found in Guangxi (pCoV-GX) shares 87% RBD and 75% RBM amino acid identity with SARS-CoV-2 (Lam et al., 2020; Zhang et al., 2020). The SARS-CoV

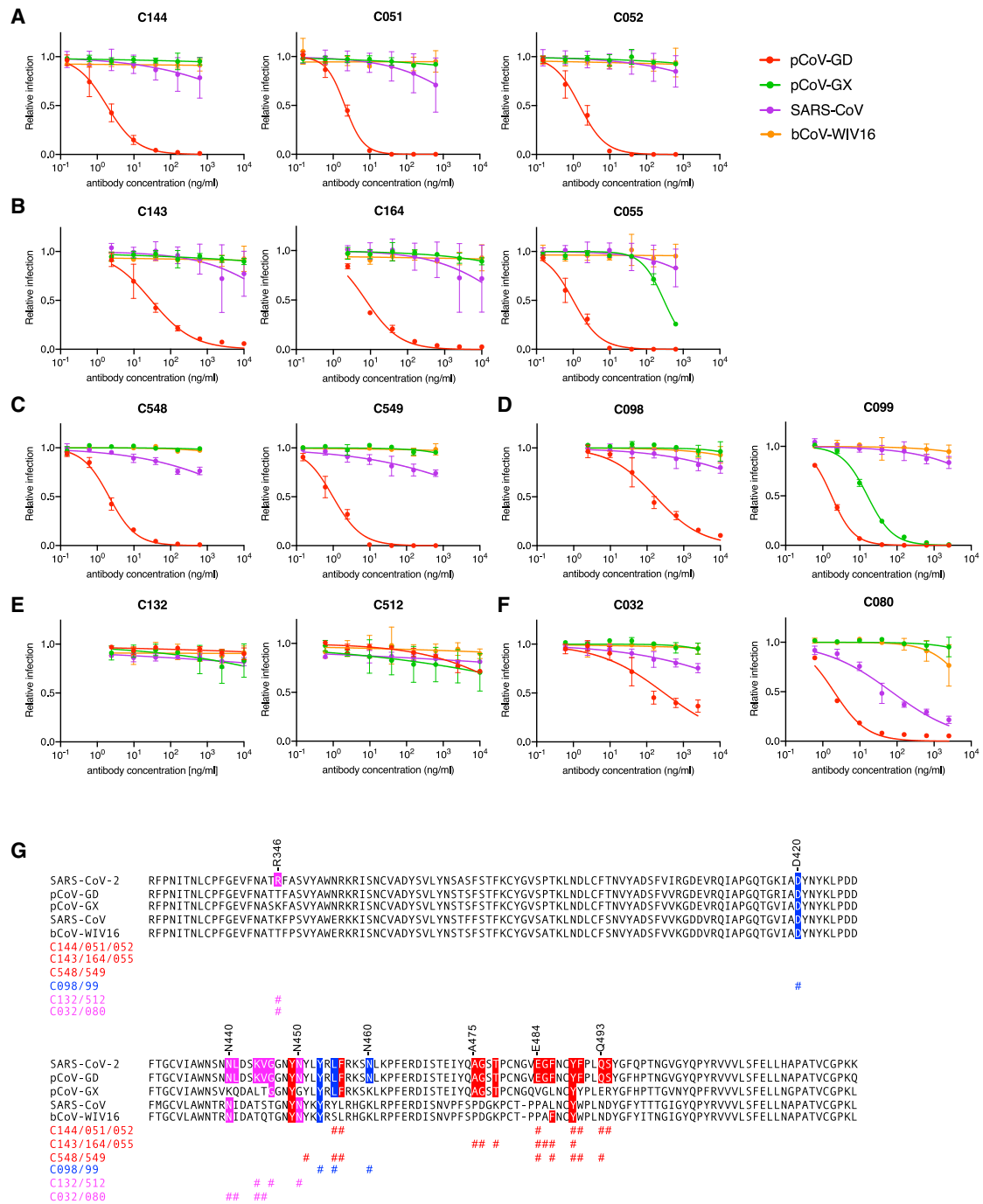


**Figure 5. Somatic mutation of SARS-CoV-2 elicited antibodies affects neutralization breadth against heterologous sarbecoviruses**

(A–F) Neutralization of HIV-1-based SARS-CoV, bat coronavirus (bCoV WIV16), or pangolin coronaviruses (pCov-GD and pCov-GX) pseudotypes by C144/C051/C052 (A), C143/C164/C055 (B), C548/C549 (C), C098/C099 (D), C132/C512 (E), and C032/C080 (F) antibodies. Mean and standard deviation of 2 independent experiments.

(G) Alignment of the heterologous sarbecovirus RBDs, with the positions and conservation of resistance mutations selected by the various clonally related antibody groups indicated by shading and hashmarks.

Spike protein is more closely related to coronaviruses found in *Rinolophus sinicus*, including bCoV-WIV16, with which it shares 94.3% RBD amino acid identity. The SARS-CoV and bat-CoV-WIV16 RBDs share 73%–75.4% identity with the

SARS-CoV-2 RBD, but only 50%–52.8% identity in the RBM (Li et al., 2005).

None of the antibodies neutralized bCoV-WIV16 pseudotypes (Figure 5A–5F). In contrast, all of the antibodies except C512

neutralized pCoV-GD pseudotypes. Some matured antibodies isolated at 6.2 months (C055, C549, C099, and C080) neutralized pCoV-GD pseudotypes more potently than their 1.3-month clonal predecessors (Figures 5B–5D, 5F), recapitulating observations with SARS-CoV-2 pseudotypes. In addition, C099, unlike its clonally related predecessor C098, potently neutralized the more distantly related pCoV-GX pseudotype ( $IC_{50} = 16$  ng/mL; Figure 5D). Finally, the 6.2-month class 3 antibody, C080, neutralized SARS-CoV ( $IC_{50} = 71$  ng/mL).

A comparison of the aligned SARS-CoV-2, pCoV-GD, pCoV-GX, SARS-CoV, and bCoV-WIV16 sequences revealed that many, but not all, of the resistance mutations selected *in vitro* coincided with residues that were variable among these sarbecoviruses, consistent with the general lack of sensitivity of the divergent viruses to the 1.3-month antibodies (Figure 5G). Nevertheless 2 of the three 6.2-month antibodies (C099 and C080) that apparently required multiple mutations for resistance, could neutralize viruses with preexisting divergence in the resistance determinants. Thus, in some cases, antibody evolution enabled neutralization of heterologous sarbecoviruses.

### Structural analyses of antibody clonal pairs reveal molecular contacts that improve potency and breadth

We investigated the effects of somatic mutations on antibody-antigen interactions by solving structures of 1.3- and 6.2-month pairs of class 1 (C098/C099) and class 2 (C144/C051) antibody Fab fragments bound to SARS-CoV-2 Spike trimers or monomeric RBDs. We also determined structures of 1.3-month class 2 (C548) and 1.3-month class 3 (C032) Fabs bound to S, allowing modeling of RBD interactions for their 6.2-month counterparts (C549 and C080, respectively) (Figures S5A–S5I; Tables S2 and S3). Across these structures, most of the substitutions found at 6.2 months post-infection occurred in complementarity-determining region (CDR) loops, in or adjacent to antibody paratopes (Figures 6A–6J, 7A–7K, S6A–S6H, and S7A–S7E).

To derive global properties of Fab-antigen interactions, we calculated shape complementarity ( $Sc$ ) indices, which vary from 0 (not complementary) to 1 (a perfect fit) and are typically 0.64–0.68 for antibody-antigen interfaces (Lawrence and Colman, 1993). For antibody pairs for which we had determined both 1.3- and 6.2-month structures,  $Sc$  values for 6.2-month antibodies were modestly increased compared with their 1.3-month counterparts: 0.56 versus 0.52 for C051 and C144 complexes with Spike, respectively ( $Sc$  values calculated for a Fab complexed with 2 adjacent RBDs), and 0.73 and 0.68 for C099 and C098 Fab complexes with RBD, respectively. Similarly, buried surface area (BSA) calculations did not reveal large increases in Fab-antigen interface areas upon antibody maturation: total BSAs for C051 and C144 interfaces were  $\sim 2,520$  and  $\sim 2,350$  Å<sup>2</sup>, respectively, and  $\sim 2,540$  and  $\sim 2,590$  Å<sup>2</sup> for C099 and C098, respectively.

To understand the influence of individual mutations on potency and viral escape, we aligned RBD-bound Fab complexes from clonally related 1.3- and 6.2-month antibodies and inspected individual residue antibody-antigen interactions (Figures 6 and S6). For the class 1 C098/C099 pair, we compared 2.0- and 2.6-Å X-ray structures of the C098-RBD and C099-CR3022-RBD complexes, respectively (Figures S5H and S5I;

Table S2). After superimposing the RBDs, the Fab  $V_H$ - $V_L$  domains adopted the same binding pose such that the CDR loops at the Fab-RBD interface were aligned equivalently (Figures 6A and 6B). Overall, the footprints of the epitope on the RBD and the paratope on the Fab were conserved (Figures S6A–S6C), which is consistent with the highly similar binding orientations of class 1 anti-RBD neutralizing antibodies (Figures S6D and S6E).

For C098 and C099, the majority of RBD contacts are mediated by CDR1 and CDR2 V gene-encoded regions (Figures S6A–S6C). Given that the C098  $V_H$  and  $V_L$  gene segment sequences contained no somatic hypermutations (Figure S6A), our structures provided the opportunity to analyze the effects of affinity maturation on the increased potency of the 6.2-month C099 antibody. Somatic mutations in C099 occurred in V gene-encoded CDR loops and framework regions (FWRs), while the CDR3 loops remained unchanged from the germline (C098) antibody (Figures S6A and S6E). As previously noted for class 1 anti-RBD neutralizing antibodies (Hurlburt et al., 2020; Tan et al., 2021), somatic mutations in the CDRH1 and CDRH2 of C099 appeared to drive improved binding and neutralizing characteristics. For example, the F271<sub>HC</sub> mutation found in C099 introduces a smaller hydrophobic residue that likely makes the CDRH1 loop more flexible, facilitating increased polar contacts and van der Waals interactions in this region (Figures 6C and 6D). In CDRH2, somatic mutations S53A<sub>HC</sub> and Y58F<sub>HC</sub> remove polar contacts with backbone carbonyl and side chain atoms at the RBD interface (Figures 6E and 6F). However, these mutations (particularly Y58F<sub>HC</sub>) increase binding affinity and neutralizing activity of class 1 anti-RBD antibodies (Tan et al., 2021), which can be partly explained by the introduction of stacking interactions with RBD residue T415 (Figure 6F). Thus, we conclude that a set of common somatic mutations found in C099 facilitates its improved neutralization potency.

For the class 2 C144/C051 antibodies, we compared our previously reported 3.2-Å cryoelectron microscopy (cryo-EM) structure of a C144 Fab-S complex (Barnes et al., 2020a) with the 3.5-Å C051-S structure reported here (Figure 6G). The C144 and C051 Fabs associate with the RBD through a similar binding mode to bridge adjacent RBDs on the surface of the S trimer (Figure 6H). As with C144, the C051 antibody heavy chain mediated the majority of RBD contacts (Figures S6F–S6H). Mutations at RBD positions L455, F456, E484, and Q493 conferred escape from C144, while only the E484K mutation conferred escape from C051 (Figure 1A). Viral escape at RBD positions L455 and Q493 is facilitated by an arginine substitution that would disrupt hydrogen-bonding networks at the C144-RBD interface (Figure 6I). Somatic mutations in the C051 CDRH1 (T28G<sub>HC</sub> and S30R<sub>HC</sub>) introduce additional polar contacts with backbone carbonyl and side chain residues at the RBD interface, while allowing additional flexibility in CDRH1 (Figure 6J), similar to observations for class 1 antibodies (Figure 6D). In addition, the CDRH3 E97D<sub>HC</sub> somatic mutation in C051 introduces a smaller charged residue that may better accommodate an arginine side chain in this region (Figure 6J). Somatic hypermutations in CDRH1 for this antibody group likely play an important role, as the clonally related C054 antibody isolated at 6.2 months is sensitive to the Q493R and L455R mutations (Gaebler et al., 2021).

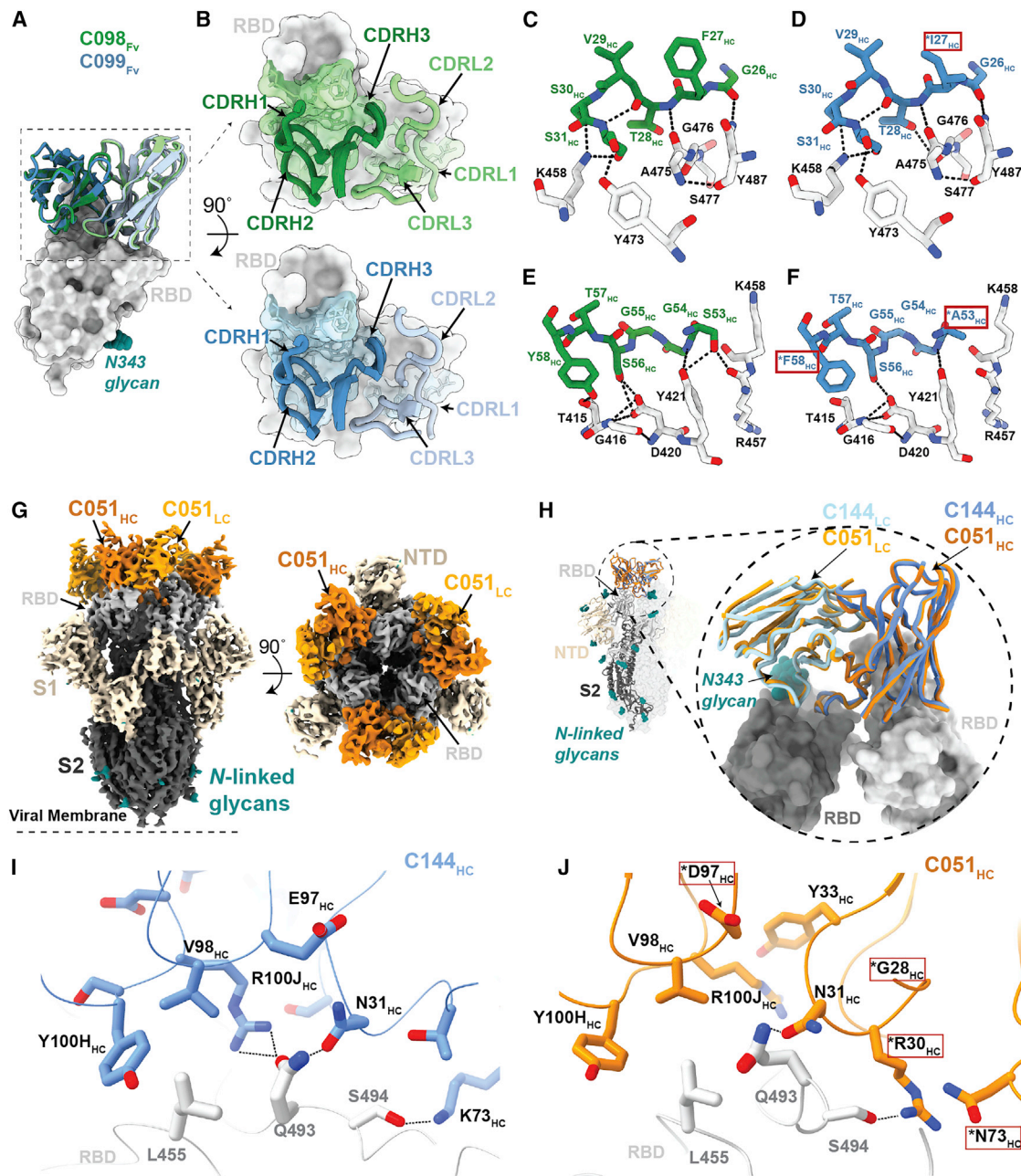


**Figure 6. Structures of class 1 and class 2 anti-RBD antibody 1.3- and 6.2-month pairs reveal maturation-induced changes in antibody-Spike contacts**

(A) Overlay of  $V_H$ - $V_L$  domains of class 1 C098 and C099 Fabs bound to RBD from 2.0 and 2.6 Å crystal structures, respectively.

(B) CDR loops of C098 and C099 mapped onto the RBD surface. Fab epitopes are colored on the RBD surface.

(C and D) Interactions of C098 (C) and C099 (D) CDRH1 residues with RBD. Residues changed by somatic hypermutation indicated by an asterisk and enclosed in a red box.

(E and F) Interactions of C098 (E) and C099 (F) CDRH2 residues with RBD. Residues changed by somatic hypermutation indicated by an asterisk and enclosed in a red box.

(G) 3.5 Å cryo-EM density for class 2 C051-S complex structure (only the  $V_H$ - $V_L$  domains of C051 are shown).

(H) Overlay of  $V_H$ - $V_L$  domains of C051 and C144 Fabs bound to S trimer. Both Fabs bridge between adjacent “down” RBDs, shown in the inset as dark and light gray surfaces.

(I and J) Interactions between RBD and C144 (I) and C051 (J) with a subset of interacting residues highlighted as sticks. Potential hydrogen bonds shown as dotted lines. Residues changed by somatic hypermutation indicated by an asterisk and enclosed in a red box.

See also [Figures S5](#) and [S6](#).

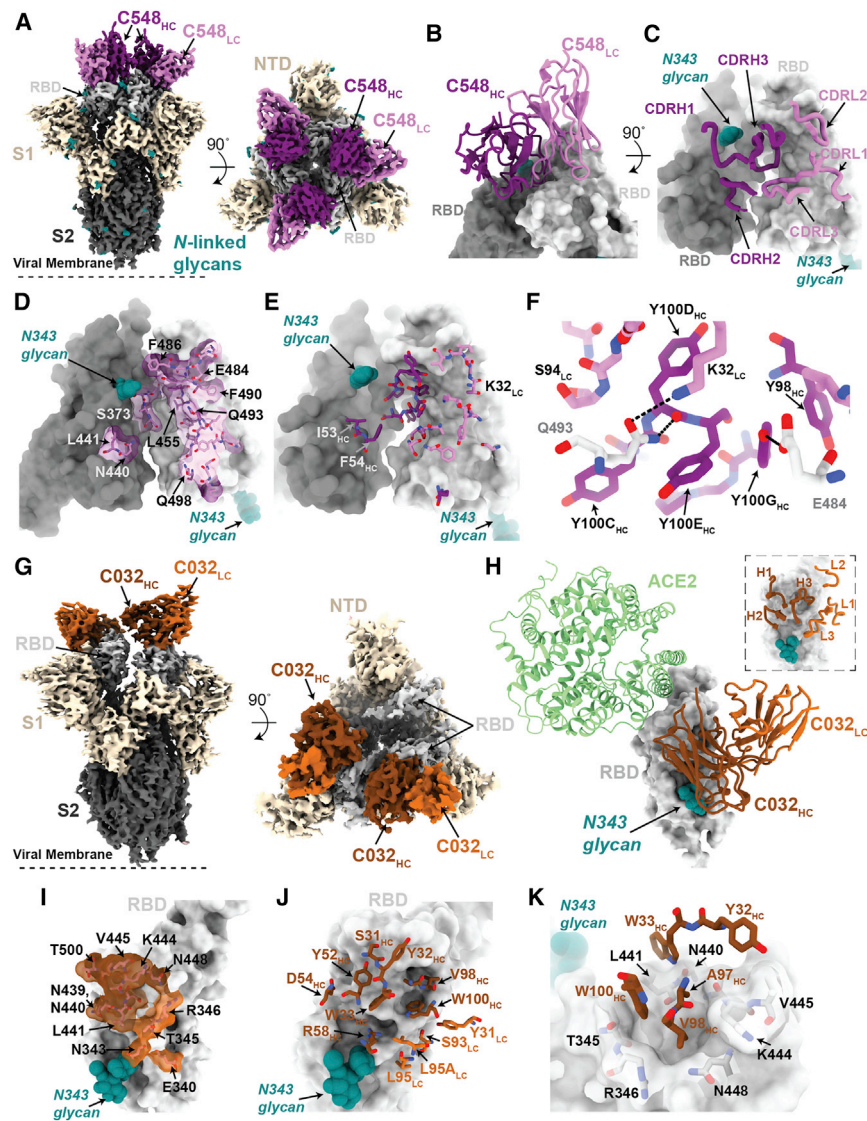


**Figure 7. Structures of class 2 and class 3 anti-RBD 1.3-month antibodies reveal structural basis for maturation-associated changes in activity**

(A) 3.4 Å cryo-EM density for class 2 C548-S complex (only the V<sub>H</sub>-V<sub>L</sub> domains of C548 are shown). (B) Close-up view of quaternary epitope involving bridging interactions between adjacent RBDs. (C) CDR loops mapped onto adjacent RBD surfaces. (D) Epitope of C548 highlighted on adjacent RBDs. (E) C548 paratope mapped onto adjacent RBDs. (F) Interactions between RBD and C548 with a subset of interacting residues highlighted as sticks. Potential hydrogen bonds shown as dotted lines. (G) 3.4 Å cryo-EM density for class 3 C032-S complex (only the V<sub>H</sub>-V<sub>L</sub> domains of C032 are shown). (H) Overlay of C032-RBD portion of the C032-S complex structure with an ACE2-RBD structure (from PDB: 6VW1). (I) Epitope of C032 highlighted on the RBD surface. (J) C032 paratope mapped onto RBD surface. (K) Interactions between RBD and C032 CDRH1 and CDRH3 loops, with a subset of interacting residues highlighted as sticks. Potential hydrogen bonds shown as dotted lines. See also [Figures S5](#) and [S7](#).

### Structures of Spike trimer complexes with 1.3-month class 2 and class 3 antibodies explain viral escape

To further understand the escape patterns of RBD-targeting antibodies, we determined cryo-EM structures of Fab-S complexes for 1.3-month class 2 (C548) and class 3 (C032) neutralizing antibodies ([Figures 7](#) and [S5](#)) and derived homology models of the 6.2-month counterparts: C549 and C080, respectively ([Figure S7](#)). In both experimentally determined structures, Fabs recognized either up or down RBD conformations ([Figure 7](#)).

The 3.4-Å cryo-EM structure of C548 Fabs bound to a closed S trimer ([Figure 7A](#)) revealed a quaternary epitope that spanned neighboring RBDs ([Figures 7B](#) and [7C](#)). The antibody paratope involved 5 of 6 CDR loops, with the majority of contacts to RBD focused on residues involved in ACE2 recognition ([Figures 7D](#) and [S7](#)). C548 is encoded by the *VH1-69* V<sub>H</sub> gene segment, which encodes a hydrophobic sequence at the tip of CDRH2 that has been shown to facilitate broad neutralization against influenza, hepatitis C, and HIV-1 ([Chen et al., 2019](#)). In C548, res-

idues I53-F54<sub>HC</sub> target a hydrophobic patch in the neighboring RBD core that resides near the base of the N343-glycan and comprises RBD residues W436, N440, and L441 ([Figures 7D](#) and [7E](#)). These interactions are akin to those observed in the C144/C051 pair, in which either Phe-Trp or Leu-Trp at the tip of CDRH3 is buried in a similar manner on the adjacent RBD ([Figures S6G](#) and [S6H](#)). These data demonstrate the convergent evolution of mechanisms for anti-RBD antibodies to target this hydrophobic patch on the RBD surface, with the potential to lock RBDs into the down position.

Viral escape from C548 was mediated by substitutions at positions L455, E484, F490, and Q493, likely due to the disruption of polar contacts at the RBD interface and/or insertion of bulky side chains into a sterically restricted region ([Figure 7F](#)). However, unlike the C144/C051 antibodies, C549 (the 6.2-month mature counterpart) maintained activity against all of the C548 viral escape mutants, including partial activity against the E484K mutant ([Figure 1D](#)). C549 exhibits accumulated somatic mutations (9 HC residues and 11 LC residues changed compared to germline) in both FWR and CDR loops ([Figure S7A](#)). Using the C548-S structure, we made a homology model of the C549-RBD interactions ([Figure S7B](#)). Light chain somatic mutations are predicted to explain the increased resistance: 30Y<sub>LC</sub> stacks against residue F490 of the RBD, while 27D<sub>LC</sub> and 92E<sub>LC</sub> increase polar contacts with the side chain N450 and backbone of F449 of RBD, respectively. ([Figure S7C](#)). While a

number of potential positions are possible, we predict that the partial retention of C549 activity against the E484K mutant likely results from a combination of increased polar and hydrophobic interactions.

To understand the impact of maturation in the C032/C080 class 3 antibody pair, we determined a 3.3-Å cryo-EM structure of a C032-S trimer complex, revealing a Fab binding orientation that does not overlap with the ACE2 binding site (Figures 7G and 7H). C032 recognizes a glycopeptidic epitope focused on a short helical segment in the RBD core that spans RBD residues 437–442 near the N343-glycan (Figure 7I), with a paratope BSA (~810 Å<sup>2</sup>) equally distributed among the CDRH1, CDRH2, CDRH3, and CDRL3 loops (Figures 7J and S7A). At the tip of CDRH3, hydrophobic residues A97HC, V98HC, and W100HC bury into a pocket shaped by RBD loops comprising residues 344–348 and 443–450 (Figure 7K), providing sequence-independent van der Waals interactions with the RBD backbone. The mutation of residues comprising this RBD pocket confers C032 resistance (Figure 3E). To predict how the affinity-matured 6.2-month antibody C080 avoids viral escape, we made a homology model of the C080-RBD structure. The majority of somatic mutations in C080 are distal to the modeled Fab-RBD interface (Figure S7D), with the exception of Y33FLC and S31IHC. I31HC fits within a hydrophobic pocket formed by V445, P499 of the RBD, and Y32HC. Thus, C080 somatic mutations likely influence both direct packing and CDR loop conformation and flexibility at the antigen interface, as has been observed for neutralizing antibodies against the HIV-1 envelope (Klein et al., 2013). C080 also acquired activity against SARS-CoV (Figure 5F). In the homology model of C080-SARS-CoV RBD, C080 somatic mutations I31HC and F33LC directly interact with RBD residues 444–445 and 346 (SARS-CoV-2 numbering), respectively, which differ between SARS-CoV-2 and SARS-CoV (Figures S7E and S7F). The CDRL3 mutations are predicted to indirectly facilitate recognition of the SARS-CoV RBD.

## DISCUSSION

Here, we describe properties of SARS-CoV-2 neutralizing antibodies that change as a consequence of accumulated somatic mutations over months in convalescent individuals (Gaebler et al., 2021; Sokal et al., 2021). Persistent somatic mutation is associated with continued availability of antigen (Victoria and Nussenzweig, 2012). For example, during chronic HIV-1 infection, antibodies develop exceptionally large numbers of mutations compared to infections of limited duration (Klein et al., 2013; Scheid et al., 2009). In SARS-CoV-2 convalescent individuals, viral proteins and nucleic acids can persist in the gut for months, providing a source of antigen to fuel germinal centers (Gaebler et al., 2021). Whether current vaccination schemes will afford a sufficient antigen persistence to elicit continued antibody maturation remains to be determined. While each antibody group had unique characteristics that were affected by somatic mutations, general themes were evident. Typically, antibodies isolated at 6.2 months had increased potency compared to their clonal relatives isolated at 1.3 months. An exception to this was C144, a particularly potent antibody, isolated at 1.3 months (Robbiani et al., 2020). Structural analysis suggests that the high potency of C144 is related to its ability to lock the S trimer in a prefusion, closed state (Barnes et al., 2020a).

Whereas antibody-producing plasma cells are selected based on their affinity for antigen, memory B cells are heterogeneous and encode a far more diverse set of antibodies with varying levels of affinity for the immunogen (Viant et al., 2020). One of the consequences of accumulating a diverse group of closely related antibody-producing cells in the memory compartment is the ability to recognize and respond to closely related pathogens (Viant et al., 2020). Consistent with this observation, an important property that was recurrently evident in the clonally related antibody groups described herein was a change in the mutations that were selected and conferred resistance to 6.2-month antibodies as compared to 1.3-month antibodies. Striking features of some of the 6.2-month antibodies included restriction of the range of options for viral escape and the retention of neutralization activity in the face of point mutations that conferred resistance to 1.3-month antibodies. The neutralization potency of certain matured antibodies, such as C549, C099, and C080, was maintained for all of the naturally circulating individual RBD substitutions tested, which is consistent with the observation of antibody antigen structures or models. In some cases, rVSV/SARS-CoV-2 selection experiments indicated that somatic mutations elevated the genetic barrier to antibody resistance, imposing a requirement for at least 2 substitutions for escape from neutralization.

The naturally circulating RBD triple mutant K417N/E484K/N501Y did not generally confer resistance to antibodies that were not already affected by the E484K mutation. This finding suggests that separate antibodies may be generally responsible for the application of selection pressure at K417, E484, and N501. Nevertheless, the E484K mutation undermined the activity of several class 2 antibodies. While a number of naturally circulating substitutions at E484 conferred resistance to some class 2 antibodies (e.g., C144, C055, C548), naturally occurring VOC often encode E484K (West et al., 2021), consistent with our finding that only the E484K substitution conferred more pervasive class 2 antibody resistance, including to some matured antibodies (e.g., C051, C052).

Similar principles, in terms of increasing breadth and potency, could apply to antibodies targeting other RBD epitopes or non-RBD epitopes such as those within the N-terminal domain. In 2 cases described here, antibody maturation enabled the neutralization of heterologous sarbecoviruses, suggesting that the development of pan-sarbecovirus vaccines may be possible (Cohen et al., 2021). The greater neutralization potency, resilience to viral mutation, and breadth of SARS-CoV-2 RBD-specific antibodies that have undergone greater degrees of somatic mutation suggests that immunization schemes that elicit higher levels of antibody mutation and diversification are desirable. Antibody maturation may be especially important as SARS-CoV-2 diversifies and adapts to the range of human antibodies elicited in vaccinated and previously infected individuals. Moreover, a diverse set of broadly neutralizing SARS-CoV-2 Spike-specific antibodies that exhibit some activity against divergent sarbecoviruses may mitigate the threat posed by this group of pandemic-threat agents.

## Limitations of the study

This study focused on representative antibodies from 3 of the 4 major classes of antibodies that target the SARS-CoV-2 RBD.

The study is not comprehensive in describing the behavior of all of the antibodies that are elicited by SARS-CoV-2 Spike, but instead illustrates the potential for increasing the effectiveness of the neutralizing antibody response through maturation. A key unknown that is not addressed in this study and is a crucial factor in determining neutralization breadth in convalescent or vaccinated individuals is the number of distinct epitopes that are targeted by SARS-CoV-2 neutralizing antibodies. The study illustrates the mutation pathways that can confer viral resistance to individual specific antibodies and antibody resilience to individual viral mutations, but the actual pathways followed in the context of natural infection may depend on the presence of other antibodies and viral variants. Finally, the optimal level of antibody mutation and the maximum breadth that is achievable through mutation of individual antibodies was not determined.

## STAR★METHODS

Detailed methods are provided in the online version of this paper and include the following:

- **KEY RESOURCES TABLE**
- **RESOURCE AVAILABILITY**
  - Lead contact
  - Materials availability
  - Data and code availability
- **EXPERIMENTAL MODEL AND SUBJECT DETAILS**
  - Cell lines
- **METHOD DETAILS**
  - Monoclonal antibodies
  - SARS-CoV-2 pseudotyped reporter virus
  - SARS-CoV-2 pseudotype neutralization assays
  - Selection of antibody resistant rVSV/SARS-CoV-2 variants
  - rVSV/SARS-CoV-2 neutralization assays
  - Sequence analyses
  - Affinity measurements
  - Protein expression and purification
  - Cryo-EM structure determinations
  - Cryo-EM structure modeling and refinement
  - X-ray structures
  - Homology modeling of Fab-RBD structures
  - Structural analyses
- **QUANTIFICATION AND STATISTICAL ANALYSIS**

## SUPPLEMENTAL INFORMATION

Supplemental information can be found online at <https://doi.org/10.1016/j.immuni.2021.07.008>.

## ACKNOWLEDGMENTS

We thank all of the study participants and clinical staff. We thank members of the Bjorkman, Nussenzweig, and Bieniasz laboratories for helpful discussions; and Dr. Jost Vielmetter, Pauline Hoffman, and the Protein Expression Center in the Beckman Institute at Caltech for expression assistance. Electron microscopy was performed in the Caltech Beckman Institute Resource Center for Transmission Electron Microscopy with assistance from Dr. Songye Chen. We thank the Gordon and Betty Moore Foundation and the Beckman Foundation for gifts to Caltech to support the Molecular Observatory (Dr. Jens Kaiser, director), and Drs. Silvia Russi, Aina Cohen, and Clyde Smith and the beamline

staff at SSRL for data collection assistance. Use of the Stanford Synchrotron Radiation Lightsource, SLAC National Accelerator Laboratory, is supported by the US Department of Energy, Office of Science, Office of Basic Energy Sciences under contract no. DE-AC02-c76SF00515. The SSRL Structural Molecular Biology Program is supported by the DOE Office of Biological and Environmental Research, and by the National Institutes of Health, National Institute of General Medical Sciences (P41GM103393). This work was supported by NIH grants R37-AI64003 (to P.D.B.), R01AI78788 (to T.H.), P01-AI138938-S1 (to P.J.B. and M.C.N.), K99 AI153465 (to A.I.F.), and 2U19AI111825 (to M.C.N.). This work was also supported by a George Mason University Fast Grant (to P.J.B.), NSF grant no. GRFP DGE-1745301 (to A.T.D.), and by the Caltech Merkin Institute for Translational Research (to P.J.B.). C.O.B. was supported by the Hanna Gray Fellowship Program from the Howard Hughes Medical Institute and the Postdoctoral Enrichment Program from the Burroughs Wellcome Fund. F.M. was supported by the Bulgari Women & Science Fellowship in COVID-19 Research. C.G. was supported by the Robert S. Wennett Post-Doctoral Fellowship, in part by the National Center for Advancing Translational Sciences (National Institutes of Health Clinical and Translational Science Award program, grant no. UL1 TR001866), and by the Shapiro-Silverberg Fund for the Advancement of Translational Research. M.C.N. and P.D.B. are Howard Hughes Medical Institute investigators. The contents of this publication are solely the responsibility of the authors and do not necessarily represent the official views of NIGMS, NIAID, or NIH.

## AUTHOR CONTRIBUTIONS

F.M., Y.W., C.O.B., F.S., M.C.N., P.J.B., T.H., and P.D.B. conceived the study and analyzed the data. F.S. and J.D.S. generated the Spike plasmids. F.M., D.S.-B., J.C.C.L., and J.D.S. performed neutralization assays with natural SARS-CoV-2 variant and sarbecovirus HIV-1 pseudotypes. Y.W., F.S., and M.R. performed the selection and characterization of escape mutants using VSV/SARS-CoV-2 and HIV-1-pseudotypes. C.O.B. and K.E.H.-T. performed the protein purification and complex assembly. A.I.F. and C.O.B. performed the crystallographic studies and analyzed structures. C.O.B., A.T.D., and A.I.F. performed the cryo-EM studies and analyzed structures. S.H. and C.A.S. generated and performed the analyses of homology models. Z.W. performed the BLI experiments. Z.W., S.F., A.C., T.Y.O., M.C., K.G.M., V.R., and A.G. isolated and characterized monoclonal antibodies. C.G. and M.C. recruited the participants and executed the clinical protocols. F.M., Y.W., C.O.B., F.S., M.C.N., P.J.B., T.H., and P.D.B. wrote the paper, with contributions from the other authors.

## DECLARATION OF INTERESTS

The Rockefeller University has filed provisional patent applications in connection with this work on which M.C.N. (US patent 63/021,387) is listed as inventor. P.D.B. has served on an advisory board to Pfizer relating to SARS-CoV-2 vaccines.

Received: March 15, 2021

Revised: May 26, 2021

Accepted: July 12, 2021

Published: July 30, 2021

## REFERENCES

- Abascal, F., Zardoya, R., and Telford, M.J. (2010). TranslatorX: multiple alignment of nucleotide sequences guided by amino acid translations. *Nucleic Acids Res.* **38**, W7–W13.
- Adams, P.D., Afonine, P.V., Bunkóczi, G., Chen, V.B., Davis, I.W., Echols, N., Headd, J.J., Hung, L.W., Kapral, G.J., Grosse-Kunstleve, R.W., et al. (2010). PHENIX: a comprehensive Python-based system for macromolecular structure solution. *Acta Crystallogr. D Biol. Crystallogr.* **66**, 213–221.
- Barnes, C.O., Jette, C.A., Abernathy, M.E., Dam, K.A., Esswein, S.R., Grinstead, H.B., Malyutin, A.G., Sharaf, N.G., Huey-Tubman, K.E., Lee, Y.E., et al. (2020a). SARS-CoV-2 neutralizing antibody structures inform therapeutic strategies. *Nature* **588**, 682–687.

- Barnes, C.O., West, A.P., Jr., Huey-Tubman, K.E., Hoffmann, M.A.G., Sharaf, N.G., Hoffman, P.R., Koranda, N., Gristick, H.B., Gaebler, C., Muecksch, F., et al. (2020b). Structures of Human Antibodies Bound to SARS-CoV-2 Spike Reveal Common Epitopes and Recurrent Features of Antibodies. *Cell* **182**, 828–842.e16.
- Battye, T.G., Kontogiannis, L., Johnson, O., Powell, H.R., and Leslie, A.G. (2011). iMOSFLM: a new graphical interface for diffraction-image processing with MOSFLM. *Acta Crystallogr. D Biol. Crystallogr.* **67**, 271–281.
- Baum, A., Fulton, B.O., Wloga, E., Copin, R., Pascal, K.E., Russo, V., Giordano, S., Lanza, K., Negron, N., Ni, M., et al. (2020). Antibody cocktail to SARS-CoV-2 spike protein prevents rapid mutational escape seen with individual antibodies. *Science* **369**, 1014–1018.
- Bowers, K.J., Chow, E., Xu, H., Dror, R.O., Eastwood, M.P., Gregersen, B.A., Klepeis, J.L., Kolossvary, I., Joraes, M.A., Sacerdoti, F.D., et al. (2006). Scalable Algorithms for Molecular Dynamics Simulations on Commodity Clusters. In *Proceedings of the ACM/IEEE Conference on Supercomputing (SC06)* (ACM/IEEE).
- Brouwer, P.J.M., Caniels, T.G., van der Straten, K., Snitselaar, J.L., Aldon, Y., Bangaru, S., Torres, J.L., Okba, N.M.A., Claireaux, M., Kerster, G., et al. (2020). Potent neutralizing antibodies from COVID-19 patients define multiple targets of vulnerability. *Science* **369**, 643–650.
- Cao, Y., Su, B., Guo, X., Sun, W., Deng, Y., Bao, L., Zhu, Q., Zhang, X., Zheng, Y., Geng, C., et al. (2020). Potent neutralizing antibodies against SARS-CoV-2 identified by high-throughput single-cell sequencing of convalescent patients' B cells. *Cell* **182**, 73–84.e16.
- Chen, F., Tzarum, N., Wilson, I.A., and Law, M. (2019). V<sub>H</sub>1-69 antiviral broadly neutralizing antibodies: genetics, structures, and relevance to rational vaccine design. *Curr. Opin. Virol.* **34**, 149–159.
- Chen, P., Nirula, A., Heller, B., Gottlieb, R.L., Boscia, J., Morris, J., Huhn, G., Cardona, J., Mocherla, B., Stosor, V., et al.; BLAZE-1 Investigators (2021). SARS-CoV-2 Neutralizing Antibody LY-CoV555 in Outpatients with Covid-19. *N. Engl. J. Med.* **384**, 229–237.
- Chen, V.B., Arendall, W.B., 3rd, Headd, J.J., Keedy, D.A., Immormino, R.M., Kapral, G.J., Murray, L.W., Richardson, J.S., and Richardson, D.C. (2010). MolProbity: all-atom structure validation for macromolecular crystallography. *Acta Crystallogr. D Biol. Crystallogr.* **66**, 12–21.
- Chen, X., Li, R., Pan, Z., Qian, C., Yang, Y., You, R., Zhao, J., Liu, P., Gao, L., Li, Z., et al. (2020). Human monoclonal antibodies block the binding of SARS-CoV-2 spike protein to angiotensin converting enzyme 2 receptor. *Cell. Mol. Immunol.* **17**, 647–649.
- Chi, X., Yan, R., Zhang, J., Zhang, G., Zhang, Y., Hao, M., Zhang, Z., Fan, P., Dong, Y., Yang, Y., et al. (2020). A neutralizing human antibody binds to the N-terminal domain of the Spike protein of SARS-CoV-2. *Science* **369**, 650–655.
- Cohen, A.A., Gnanaprasadam, P.N.P., Lee, Y.E., Hoffman, P.R., Ou, S., Kakutani, L.M., Keeffe, J.R., Wu, H.-J., Howarth, M., West, A.P., et al. (2021). Mosaic nanoparticles elicit cross-reactive immune responses to zoonotic coronaviruses in mice. *Science* **371**, 735–741.
- DeWitt, W.S., 3rd, Mesin, L., Victora, G.D., Minin, V.N., and Matsen, F.A., 4th (2018). Using Genotype Abundance to Improve Phylogenetic Inference. *Mol. Biol. Evol.* **35**, 1253–1265.
- Elbe, S., and Buckland-Merrett, G. (2017). Data, disease and diplomacy: GISAID's innovative contribution to global health. *Glob Chall* **1**, 33–46.
- Emsley, P., Lohkamp, B., Scott, W.G., and Cowtan, K. (2010). Features and development of Coot. *Acta Crystallogr. D Biol. Crystallogr.* **66**, 486–501.
- Fujino, T., Nomoto, H., Kutsuna, S., Ujii, M., Suzuki, T., Sato, R., Fujimoto, T., Kuroda, M., Wakita, T., and Ohmagari, N. (2021). Novel SARS-CoV-2 Variant Identified in Travelers from Brazil to Japan. *Emerg. Infect. Dis.* **27**, 1243–1245.
- Gaebler, C., Lorenzi, J.C.C., Oliveira, T.Y., Nogueira, L., Ramos, V., Lu, C.L., Pai, J.A., Mendoza, P., Jankovic, M., Caskey, M., and Nussenzweig, M.C. (2019). Combination of quadruplex qPCR and next-generation sequencing for qualitative and quantitative analysis of the HIV-1 latent reservoir. *J. Exp. Med.* **216**, 2253–2264.
- Gaebler, C., Wang, Z., Lorenzi, J.C.C., Muecksch, F., Finkin, S., Tokuyama, M., Cho, A., Jankovic, M., Schaefer-Babajew, D., Oliveira, T.Y., et al. (2021). Evolution of antibody immunity to SARS-CoV-2. *Nature* **591**, 639–644.
- Goddard, T.D., Huang, C.C., Meng, E.C., Pettersen, E.F., Couch, G.S., Morris, J.H., and Ferrin, T.E. (2018). UCSF ChimeraX: meeting modern challenges in visualization and analysis. *Protein Sci.* **27**, 14–25.
- Greaney, A.J., Loes, A.N., Crawford, K.H.D., Starr, T.N., Malone, K.D., Chu, H.Y., and Bloom, J.D. (2021). Comprehensive mapping of mutations in the SARS-CoV-2 receptor-binding domain that affect recognition by polyclonal human plasma antibodies. *Cell Host Microbe* **29**, 463–476.e6.
- Hansen, J., Baum, A., Pascal, K.E., Russo, V., Giordano, S., Wloga, E., Fulton, B.O., Yan, Y., Koon, K., Patel, K., et al. (2020). Studies in humanized mice and convalescent humans yield a SARS-CoV-2 antibody cocktail. *Science* **369**, 1010–1014.
- Hsieh, C.L., Goldsmith, J.A., Schaub, J.M., DiVenere, A.M., Kuo, H.C., Javanmardi, K., Le, K.C., Wrapp, D., Lee, A.G., Liu, Y., et al. (2020). Structure-based design of prefusion-stabilized SARS-CoV-2 spikes. *Science* **369**, 1501–1505.
- Hurlburt, N.K., Seydoux, E., Wan, Y.H., Edara, V.V., Stuart, A.B., Feng, J., Suthar, M.S., McGuire, A.T., Stamatatos, L., and Pancera, M. (2020). Structural basis for potent neutralization of SARS-CoV-2 and role of antibody affinity maturation. *Nat. Commun.* **11**, 5713.
- Ju, B., Zhang, Q., Ge, J., Wang, R., Sun, J., Ge, X., Yu, J., Shan, S., Zhou, B., Song, S., et al. (2020). Human neutralizing antibodies elicited by SARS-CoV-2 infection. *Nature* **584**, 115–119.
- Kabsch, W. (2010). XDS. *Acta Crystallogr. D Biol. Crystallogr.* **66**, 125–132.
- Klein, F., Diskin, R., Scheid, J.F., Gaebler, C., Mouquet, H., Georgiev, I.S., Pancera, M., Zhou, T., Incesu, R.B., Fu, B.Z., et al. (2013). Somatic mutations of the immunoglobulin framework are generally required for broad and potent HIV-1 neutralization. *Cell* **153**, 126–138.
- Kreer, C., Zehner, M., Weber, T., Ercanoglu, M.S., Gieselmann, L., Rohde, C., Halwe, S., Korenkov, M., Schommers, P., Vanshylla, K., et al. (2020). Longitudinal Isolation of Potent Near-Germline SARS-CoV-2-Neutralizing Antibodies from COVID-19 Patients. *Cell* **182**, 843–854.e12.
- Krissinel, E., and Henrick, K. (2007). Inference of macromolecular assemblies from crystalline state. *J. Mol. Biol.* **372**, 774–797.
- Lam, T.T., Jia, N., Zhang, Y.W., Shum, M.H., Jiang, J.F., Zhu, H.C., Tong, Y.G., Shi, Y.X., Ni, X.B., Liao, Y.S., et al. (2020). Identifying SARS-CoV-2-related coronaviruses in Malayan pangolins. *Nature* **583**, 282–285.
- Lawrence, M.C., and Colman, P.M. (1993). Shape complementarity at protein/protein interfaces. *J. Mol. Biol.* **234**, 946–950.
- Leaver-Fay, A., Tyka, M., Lewis, S.M., Lange, O.F., Thompson, J., Jacak, R., Kaufman, K., Renfrew, P.D., Smith, C.A., Sheffler, W., et al. (2011). ROSETTA3: an object-oriented software suite for the simulation and design of macromolecules. *Methods Enzymol.* **487**, 545–574.
- Lefranc, M.P. (2011). IMGT, the International ImMunoGeneTics Information System. *Cold Spring Harb. Protoc.* **2011**, 595–603.
- Lefranc, M.P., Giudicelli, V., Duroux, P., Jabado-Michaloud, J., Folch, G., Aouinti, S., Carillon, E., Duvergey, H., Houles, A., Paysan-Lafosse, T., et al. (2015). IMGT®, the international ImMunoGeneTics information system® 25 years on. *Nucleic Acids Res.* **43**, D413–D422.
- Li, W., Shi, Z., Yu, M., Ren, W., Smith, C., Epstein, J.H., Wang, H., Crameri, G., Hu, Z., Zhang, H., et al. (2005). Bats are natural reservoirs of SARS-like coronaviruses. *Science* **310**, 676–679.
- Liu, Z., VanBlargan, L.A., Bloyet, L.M., Rothlauf, P.W., Chen, R.E., Stumpf, S., Zhao, H., Errico, J.M., Theel, E.S., Liebeskind, M.J., et al. (2021). Identification of SARS-CoV-2 spike mutations that attenuate monoclonal and serum antibody neutralization. *Cell Host Microbe* **29**, 477–488.e4.
- Luchsinger, L.L., Ransegnola, B.P., Jin, D.K., Muecksch, F., Weisblum, Y., Bao, W., George, P.J., Rodriguez, M., Tricoche, N., Schmidt, F., et al. (2020). Serological Assays Estimate Highly Variable SARS-CoV-2 Neutralizing Antibody Activity in Recovered COVID-19 Patients. *J. Clin. Microbiol.* **58**, e02005-20.

- Mastrorarde, D.N. (2005). Automated electron microscope tomography using robust prediction of specimen movements. *J. Struct. Biol.* 152, 36–51.
- Muecksch, F., Wise, H., Batchelor, B., Squires, M., Semple, E., Richardson, C., McGuire, J., Clearly, S., Furrie, E., Greig, N., et al. (2021). Longitudinal analysis of serology and neutralizing antibody levels in COVID19 convalescents. *J. Infect. Dis.* 223, 389–398.
- Pear, W.S., Nolan, G.P., Scott, M.L., and Baltimore, D. (1993). Production of high-titer helper-free retroviruses by transient transfection. *Proc Natl Acad Sci U S A*. <https://doi.org/10.1073/pnas.90.18.8392>.
- Plotkin, S.A. (2010). Correlates of protection induced by vaccination. *Clin. Vaccine Immunol.* 17, 1055–1065.
- Punjani, A., Rubinstein, J.L., Fleet, D.J., and Brubaker, M.A. (2017). cryoSPARC: algorithms for rapid unsupervised cryo-EM structure determination. *Nat. Methods* 14, 290–296.
- Robbiani, D.F., Gaebler, C., Muecksch, F., Lorenzi, J.C.C., Wang, Z., Cho, A., Agudelo, M., Barnes, C.O., Gazumyan, A., Finkin, S., et al. (2020). Convergent antibody responses to SARS-CoV-2 in convalescent individuals. *Nature* 584, 437–442.
- Rogers, T.F., Zhao, F., Huang, D., Beutler, N., Burns, A., He, W.T., Limbo, O., Smith, C., Song, G., Woehl, J., et al. (2020). Isolation of potent SARS-CoV-2 neutralizing antibodies and protection from disease in a small animal model. *Science* 369, 956–963.
- Sahin, U., Muik, A., Derhovanessian, E., Vogler, I., Kranz, L.M., Vormehr, M., Baum, A., Pascal, K., Quandt, J., Maurus, D., et al. (2020). COVID-19 vaccine BNT162b1 elicits human antibody and T<sub>H</sub>1 T cell responses. *Nature* 586, 594–599.
- Sakharkar, M., Rappazzo, C.G., Wieland-Alter, W.F., Hsieh, C.L., Wrapp, D., Esterman, E.S., Kaku, C.I., Wec, A.Z., Geoghegan, J.C., McLellan, J.S., et al. (2021). Prolonged evolution of the human B cell response to SARS-CoV-2 infection. *Sci. Immunol.* 6, eabg6916.
- Sali, A., and Blundell, T.L. (1993). Comparative protein modelling by satisfaction of spatial restraints. *J. Mol. Biol.* 234, 779–815.
- Sastry, G.M., Adzhigirey, M., Day, T., Annabhimoju, R., and Sherman, W. (2013). Protein and ligand preparation: parameters, protocols, and influence on virtual screening enrichments. *J. Comput. Aided Mol. Des.* 27, 221–234.
- Scheid, J.F., Mouquet, H., Feldhahn, N., Seaman, M.S., Velinzon, K., Pietzsch, J., Ott, R.G., Anthony, R.M., Zebroski, H., Hurley, A., et al. (2009). Broad diversity of neutralizing antibodies isolated from memory B cells in HIV-infected individuals. *Nature* 458, 636–640.
- Scheres, S.H., and Chen, S. (2012). Prevention of overfitting in cryo-EM structure determination. *Nat. Methods* 9, 853–854.
- Schmidt, F., Weisblum, Y., Muecksch, F., Hoffmann, H.H., Michailidis, E., Lorenzi, J.C.C., Mendoza, P., Rutkowska, M., Bednarski, E., Gaebler, C., et al. (2020). Measuring SARS-CoV-2 neutralizing antibody activity using pseudotyped and chimeric viruses. *J. Exp. Med.* 217, e20201181.
- Seow, J., Graham, C., Merrick, B., Acors, S., Pickering, S., Steel, K.J.A., Hemmings, O., O’Byrne, A., Kouphou, N., Galao, R.P., et al. (2020). Longitudinal observation and decline of neutralizing antibody responses in the three months following SARS-CoV-2 infection in humans. *Nat. Microbiol.* 5, 1598–1607.
- Seydoux, E., Homad, L.J., MacCamy, A.J., Parks, K.R., Hurlburt, N.K., Jennewein, M.F., Akins, N.R., Stuart, A.B., Wan, Y.H., Feng, J., et al. (2020). Analysis of a SARS-CoV-2-Infected Individual Reveals Development of Potent Neutralizing Antibodies with Limited Somatic Mutation. *Immunity* 53, 98–105.e5.
- Shi, R., Shan, C., Duan, X., Chen, Z., Liu, P., Song, J., Song, T., Bi, X., Han, C., Wu, L., et al. (2020). A human neutralizing antibody targets the receptor-binding site of SARS-CoV-2. *Nature* 584, 120–124.
- Shu, Y., and McCauley, J. (2017). GISAID: Global initiative on sharing all influenza data - from vision to reality. *Euro Surveill.* <https://doi.org/10.2807/1560-7917.ES.2017.22.13.30494>.
- Sokal, A., Chappert, P., Barba-Spaeth, G., Roeser, A., Fourati, S., Azzouli, I., Vandenberghe, A., Fernandez, I., Meola, A., Bouvier-Alias, M., et al. (2021). Maturation and persistence of the anti-SARS-CoV-2 memory B cell response. *Cell* 184, 1201–1213.e14.
- Tan, T.J.C., Yuan, M., Kuzelka, K., Padron, G.C., Beal, J.R., Chen, X., Wang, Y., Rivera-Cardona, J., Zhu, X., Stadtmueller, B.M., et al. (2021). Sequence signatures of two IGHV3-53/3-66 public clonotypes to SARS-CoV-2 receptor binding domain. *bioRxiv*. <https://doi.org/10.1101/2021.01.26.428356>.
- Tegally, H., Wilkinson, E., Giovanetti, M., Iranzadeh, A., Fonseca, V., Giandhari, J., Doolabh, D., Pillay, S., San, E.J., Msomi, N., et al. (2020). Emergence and rapid spread of a new severe acute respiratory syndrome-related coronavirus 2 (SARS-CoV-2) lineage with multiple spike mutations in South Africa. *medRxiv*, 2020.2012.2021.20248640.
- Terwilliger, T.C., Adams, P.D., Afonine, P.V., and Sobolev, O.V. (2018). A fully automatic method yielding initial models from high-resolution cryo-electron microscopy maps. *Nat. Methods* 15, 905–908.
- Tortorici, M.A., Beltramello, M., Lempp, F.A., Pinto, D., Dang, H.V., Rosen, L.E., McCallum, M., Bowen, J., Minola, A., Jaconi, S., et al. (2020). Ultrapotent human antibodies protect against SARS-CoV-2 challenge via multiple mechanisms. *Science* 370, 950–957.
- Viant, C., Weymar, G.H.J., Escolano, A., Chen, S., Hartweg, H., Cipolla, M., Gazumyan, A., and Nussenzweig, M.C. (2020). Antibody Affinity Shapes the Choice between Memory and Germinal Center B Cell Fates. *Cell* 183, 1298–1311.e11.
- Victoria, G.D., and Nussenzweig, M.C. (2012). Germinal centers. *Annu. Rev. Immunol.* 30, 429–457.
- Volz, E., Mishra, S., Chand, M., Barrett, J.C., Johnson, R., Geidelberg, L., Hinsley, W.R., Laydon, D.J., Dabrera, G., O’Toole, Á., et al. (2021). Transmission of SARS-CoV-2 Lineage B.1.1.7 in England: insights from linking epidemiological and genetic data. *medRxiv*. <https://doi.org/10.1101/2020.12.30.20249034>.
- Walls, A.C., Park, Y.J., Tortorici, M.A., Wall, A., McGuire, A.T., and Veesler, D. (2020). Structure, Function, and Antigenicity of the SARS-CoV-2 Spike Glycoprotein. *Cell* 181, 281–292.e6.
- Wang, Z., Muecksch, F., Schaefer-Babajew, D., Finkin, S., Viant, C., Gaebler, C., Barnes, C., Cipolla, M., Ramos, V., Oliveira, T.Y., et al. (2021a). Naturally enhanced neutralizing breadth against SARS-CoV-2 after one year. *Nature* 595, 426–431. <https://doi.org/10.1038/s41586-021-03696-9>.
- Wang, Z., Schmidt, F., Weisblum, Y., Muecksch, F., Barnes, C.O., Finkin, S., Schaefer-Babajew, D., Cipolla, M., Gaebler, C., Lieberman, J.A., et al. (2021b). mRNA vaccine-elicited antibodies to SARS-CoV-2 and circulating variants. *Nature* 592, 616–622.
- Wec, A.Z., Wrapp, D., Herbert, A.S., Maurer, D.P., Haslwanter, D., Sakharkar, M., Jangra, R.K., Dieterle, M.E., Lilov, A., Huang, D., et al. (2020). Broad neutralization of SARS-related viruses by human monoclonal antibodies. *Science* 369, 731–736.
- Weinreich, D.M., Sivapalasingam, S., Norton, T., Ali, S., Gao, H., Bhore, R., Musser, B.J., Soo, Y., Rofail, D., Im, J., et al.; Trial Investigators (2021). REGN-COV2, a Neutralizing Antibody Cocktail, in Outpatients with Covid-19. *N. Engl. J. Med.* 384, 238–251.
- Weisblum, Y., Schmidt, F., Zhang, F., DaSilva, J., Poston, D., Lorenzi, J.C., Muecksch, F., Rutkowska, M., Hoffmann, H.H., Michailidis, E., et al. (2020). Escape from neutralizing antibodies by SARS-CoV-2 spike protein variants. *eLife* 9, e61312.
- West, A.P., Barnes, C.O., Yang, Z., and Bjorkman, P.J. (2021). SARS-CoV-2 lineage B.1.526 emerging in the New York region detected by software utility created to query the spike mutational landscape. *bioRxiv*, 2021.2002.2014.431043.
- Wibmer, C.K., Ayres, F., Hermanus, T., Madzivhandila, M., Kgagudi, P., Lambson, B.E., Vermeulen, M., van den Berg, K., Rossouw, T., Boswell, M., et al. (2021). SARS-CoV-2 501Y.V2 escapes neutralization by South African COVID-19 donor plasma. *bioRxiv*, 2021.2001.2018.427166.
- Widge, A.T., Roupheal, N.G., Jackson, L.A., Anderson, E.J., Roberts, P.C., Makhene, M., Chappell, J.D., Denison, M.R., Stevens, L.J., Pruijssers, A.J., et al.; mRNA-1273 Study Group (2021). Durability of Responses after SARS-CoV-2 mRNA-1273 Vaccination. *N. Engl. J. Med.* 384, 80–82.

- Winn, M.D., Ballard, C.C., Cowtan, K.D., Dodson, E.J., Emsley, P., Evans, P.R., Keegan, R.M., Krissinel, E.B., Leslie, A.G., McCoy, A., et al. (2011). Overview of the CCP4 suite and current developments. *Acta Crystallogr. D Biol. Crystallogr.* 67, 235–242.
- Wrapp, D., Wang, N., Corbett, K.S., Goldsmith, J.A., Hsieh, C.L., Abiona, O., Graham, B.S., and McLellan, J.S. (2020). Cryo-EM structure of the 2019-nCoV spike in the prefusion conformation. *Science* 367, 1260–1263.
- Wu, F., Wang, A., Liu, M., Wang, Q., Chen, J., Xia, S., Ling, Y., Zhang, Y., Xun, J., Lu, L., et al. (2020a). Neutralizing antibody responses to SARS-CoV-2 in a COVID-19 recovered patient cohort and their implications. medRxiv. <https://doi.org/10.1101/2020.03.30.20047365>.
- Wu, Y., Wang, F., Shen, C., Peng, W., Li, D., Zhao, C., Li, Z., Li, S., Bi, Y., Yang, Y., et al. (2020b). A non-competing pair of human neutralizing antibodies block COVID-19 virus binding to its receptor ACE2. *Science* 368, 1274–1278.
- Wu, Y., Wang, F., Shen, C., Peng, W., Li, D., Zhao, C., Li, Z., Li, S., Bi, Y., Yang, Y., et al. (2020c). A noncompeting pair of human neutralizing antibodies block COVID-19 virus binding to its receptor ACE2. *Science* 368, 1274–1278.
- Yuan, M., Liu, H., Wu, N.C., Lee, C.D., Zhu, X., Zhao, F., Huang, D., Yu, W., Hua, Y., Tien, H., et al. (2020). Structural basis of a shared antibody response to SARS-CoV-2. *Science* 369, 1119–1123.
- Zhang, T., Wu, Q., and Zhang, Z. (2020). Probable Pangolin Origin of SARS-CoV-2 Associated with the COVID-19 Outbreak. *Curr. Biol.* 30, 1346–1351.e2.
- Zhou, P., Yang, X.L., Wang, X.G., Hu, B., Zhang, L., Zhang, W., Si, H.R., Zhu, Y., Li, B., Huang, C.L., et al. (2020). A pneumonia outbreak associated with a new coronavirus of probable bat origin. *Nature* 579, 270–273.
- Zost, S.J., Gilchuk, P., Case, J.B., Binshtein, E., Chen, R.E., Reidy, J.X., Trivette, A., Nargi, R.S., Sutton, R.E., Suryadevara, N., et al. (2020). Potently neutralizing human antibodies that block SARS-CoV-2 receptor binding and protect animals. bioRxiv. <https://doi.org/10.1101/2020.05.22.111005>.

STAR★METHODS

KEY RESOURCES TABLE

REAGENT or RESOURCE	SOURCE	IDENTIFIER
<b>Antibodies</b>		
C032	Robbiani et al., 2020	<a href="https://doi.org/10.1038/s41586-020-2456-9">https://doi.org/10.1038/s41586-020-2456-9</a>
C051	Gaebler et al., 2021	<a href="https://doi.org/10.1038/s41586-021-03207-w">doi.org/10.1038/s41586-021-03207-w</a>
C052	Gaebler et al., 2021	<a href="https://doi.org/10.1038/s41586-021-03207-w">doi.org/10.1038/s41586-021-03207-w</a>
C055	Gaebler et al., 2021	<a href="https://doi.org/10.1038/s41586-021-03207-w">doi.org/10.1038/s41586-021-03207-w</a>
C080	Gaebler et al., 2021	<a href="https://doi.org/10.1038/s41586-021-03207-w">doi.org/10.1038/s41586-021-03207-w</a>
C098	Gaebler et al., 2021	<a href="https://doi.org/10.1038/s41586-021-03207-w">doi.org/10.1038/s41586-021-03207-w</a>
C099	Gaebler et al., 2021	<a href="https://doi.org/10.1038/s41586-021-03207-w">doi.org/10.1038/s41586-021-03207-w</a>
C132	Robbiani et al., 2020	<a href="https://doi.org/10.1038/s41586-020-2456-9">https://doi.org/10.1038/s41586-020-2456-9</a>
C143	Robbiani et al., 2020	<a href="https://doi.org/10.1038/s41586-020-2456-9">https://doi.org/10.1038/s41586-020-2456-9</a>
C144	Robbiani et al., 2020	<a href="https://doi.org/10.1038/s41586-020-2456-9">https://doi.org/10.1038/s41586-020-2456-9</a>
C164	Robbiani et al., 2020	<a href="https://doi.org/10.1038/s41586-020-2456-9">https://doi.org/10.1038/s41586-020-2456-9</a>
C512	Gaebler et al., 2021	<a href="https://doi.org/10.1038/s41586-021-03207-w">doi.org/10.1038/s41586-021-03207-w</a>
C548	Gaebler et al., 2021	<a href="https://doi.org/10.1038/s41586-021-03207-w">doi.org/10.1038/s41586-021-03207-w</a>
C549	Gaebler et al., 2021	<a href="https://doi.org/10.1038/s41586-021-03207-w">doi.org/10.1038/s41586-021-03207-w</a>
<b>Bacterial and virus strains</b>		
rVSV/SARS-CoV-2/GFP <sub>1D7</sub>	Schmidt et al., 2020	<a href="https://doi.org/10.1084/jem.20201181">https://doi.org/10.1084/jem.20201181</a>
rVSV/SARS-CoV-2/GFP <sub>2E1</sub>	Schmidt et al., 2020	<a href="https://doi.org/10.1084/jem.20201181">https://doi.org/10.1084/jem.20201181</a>
K444T <sub>2E1</sub>	Weisblum et al., 2020	DOI: 10.7554/eLife.61312
F486S <sub>2E1</sub>	This paper	N/A
T478R <sub>2E1</sub>	This paper	N/A
D420Y_N460H <sub>1D7</sub>	This paper	N/A
D420Y <sub>1D7</sub>	This paper	N/A
Y453H_L455R <sub>2E1</sub>	This paper	N/A
Y449H_E484K <sub>1D7</sub>	This paper	N/A
F486L_F490P <sub>2E1</sub>	This paper	N/A
G485S <sub>1D7</sub>	This paper	N/A
L441Q_H245R <sub>2E1</sub>	This paper	N/A
F486V <sub>2E1</sub>	This paper	N/A
K444E <sub>1D7</sub>	This paper	N/A
N460Y <sub>2E1</sub>	This paper	N/A
L455R <sub>2E1</sub>	This paper	N/A
E484K <sub>2E1</sub>	Weisblum et al., 2020	<a href="https://doi.org/10.7554/eLife.61312">https://doi.org/10.7554/eLife.61312</a>
<b>Chemicals, peptides, and recombinant proteins</b>		
SARS-CoV-2 RBD	Robbiani et al., 2020	<a href="https://doi.org/10.1038/s41586-020-2456-9">https://doi.org/10.1038/s41586-020-2456-9</a>
SARS-CoV-2 RBD E484K mutant	Wang et al., 2021b	<a href="https://doi.org/10.1038/s41586-021-03324-6">https://doi.org/10.1038/s41586-021-03324-6</a>
SARS-CoV-2 RBD Q493R mutant	Wang et al., 2021b	<a href="https://doi.org/10.1038/s41586-021-03324-6">https://doi.org/10.1038/s41586-021-03324-6</a>
SARS-CoV-2 RBD R346S mutant	Wang et al., 2021b	<a href="https://doi.org/10.1038/s41586-021-03324-6">https://doi.org/10.1038/s41586-021-03324-6</a>
SARS-CoV-2 RBD N440K mutant	Wang et al., 2021b	<a href="https://doi.org/10.1038/s41586-021-03324-6">https://doi.org/10.1038/s41586-021-03324-6</a>
SARS-CoV-2 RBD KEN mutant	Wang et al., 2021a	<a href="https://doi.org/10.1038/s41586-021-03696-9">https://doi.org/10.1038/s41586-021-03696-9</a>
Dulbecco's Modified Eagle Medium (DMEM)	GIBCO	Cat#11995-065
FBS	Sigma	Cat#F0926
Polyethylenimine	Polysciences	Cat#23966-1; CAS: 9002-98-6, 26913-06-4
Gentamicin solution	Sigma-Aldrich	Cat#G1397; CAS:1405-41-0
Blasticidin S HCl	GIBCO	Cat#A1113902; CAS: 3513-03-9

(Continued on next page)

**Continued**

REAGENT or RESOURCE	SOURCE	IDENTIFIER
<b>Critical commercial assays</b>		
Luciferase Cell Culture Lysis 5X Reagent	Promega	Cat#E1531
Protein A biosensor	ForteBio	Cat#18-5010
Bio-Layer Interferometer	ForteBio	Octet RED96e
Nano-Glo Luciferase Assay System	Promega	Cat#N1110
<b>Deposited data</b>		
X-ray crystal coordinates C032 Fab	This paper	PDB: 7N3E
X-ray crystal coordinates C080 Fab	This paper	PDB: 7N3F
X-ray crystal coordinates C098 Fab	This paper	PDB: 7N3G
X-ray crystal coordinates C099 Fab	This paper	PDB: 7N3H
X-ray crystal coordinates C098-RBD complex	This paper	PDB: 7N3I
X-ray crystal coordinates C099-CR3022-RBD complex	This paper	PDB: 7R8L
Cryo-EM coordinates and maps C032-S 6P complex	This paper	PDB: 7R8M; EMDB: 24318
Cryo-EM coordinates and maps C051-S 6P complex	This paper	PDB: 7R8N; EMDB: 24319
Cryo-EM coordinates and maps C548-S 6P complex	This paper	PDB: 7R8O; EMDB: 24320
<b>Experimental models: Cell lines</b>		
293T cells (XX)	<a href="#">Pear et al., 1993</a>	Cat#CCLV-RIE 1018; RRID: CVCL_0063
293T/Ace2 cells (XX)	<a href="#">Robbiani et al., 2020</a>	<a href="https://doi.org/10.1038/s41586-020-2456-9">https://doi.org/10.1038/s41586-020-2456-9</a>
293TAce2 cells cl.22 (XX)	<a href="#">Schmidt et al., 2020</a>	<a href="https://doi.org/10.1084/jem.20201181">https://doi.org/10.1084/jem.20201181</a>
HT1080Ace2 cells cl.14 (XY)	<a href="#">Schmidt et al., 2020</a>	<a href="https://doi.org/10.1084/jem.20201181">https://doi.org/10.1084/jem.20201181</a>
<b>Recombinant DNA</b>		
pNL4-3DEnv-nanoluc	<a href="#">Robbiani et al., 2020</a>	<a href="https://doi.org/10.1038/s41586-020-2456-9">https://doi.org/10.1038/s41586-020-2456-9</a>
pCR3.1_GA_S2_Wuhan (pSARS-CoV2-S <sub>trunc</sub> )	<a href="#">Robbiani et al., 2020</a> <a href="#">Schmidt et al., 2020</a>	<a href="https://doi.org/10.1038/s41586-020-2456-9">https://doi.org/10.1038/s41586-020-2456-9</a> <a href="https://doi.org/10.1084/jem.20201181">https://doi.org/10.1084/jem.20201181</a>
pCR3.1_GA_S2_D420Y	This paper	N/A
pCR3.1_GA_S2_N460H	This paper	N/A
pCR3.1_GA_S2_D420Y_N460H	This paper	N/A
pCR3.1_GA_S2_F490P	This paper	N/A
pCR3.1_GA_S2_Y453H	This paper	N/A
pCR3.1_GA_S2_F486L	This paper	N/A
pCR3.1_GA_S2_L455R_Y453H	This paper	N/A
pCR3.1_GA_S2_Y449H_R683G	This paper	N/A
pCR3.1_GA_S2_Y449H_E484K_R683G	This paper	N/A
pCR3.1_GA_S2_F486L_F490P	This paper	N/A
pCR3.1_GA_S2_E484K_R683G	<a href="#">Wang et al., 2021b</a>	<a href="https://doi.org/10.1038/s41586-021-03324-6">https://doi.org/10.1038/s41586-021-03324-6</a>
pCR3.1_GA_S2_R683G	<a href="#">Wang et al., 2021b</a>	<a href="https://doi.org/10.1101/2021.01.15.426911">https://doi.org/10.1101/2021.01.15.426911</a>
pCR3.1_GA_S2_K417N_E484K_N501Y	<a href="#">Wang et al., 2021b</a>	<a href="https://doi.org/10.1101/2021.01.15.426911">https://doi.org/10.1101/2021.01.15.426911</a>
pCR3.1_GA_S2_R346S	<a href="#">Weisblum et al., 2020</a>	<a href="https://doi.org/10.7554/eLife.61312">https://doi.org/10.7554/eLife.61312</a>
pCR3.1_GA_S2_V367F	<a href="#">Weisblum et al., 2020</a>	<a href="https://doi.org/10.7554/eLife.61312">https://doi.org/10.7554/eLife.61312</a>
pCR3.1_GA_S2_R403K	This paper	N/A
pCR3.1_GA_S2_K417N	<a href="#">Wang et al., 2021b</a>	<a href="https://doi.org/10.1038/s41586-021-03324-6">https://doi.org/10.1038/s41586-021-03324-6</a>
pCR3.1_GA_S2_N439K	<a href="#">Weisblum et al., 2020</a>	<a href="https://doi.org/10.7554/eLife.61312">https://doi.org/10.7554/eLife.61312</a>
pCR3.1_GA_S2_N440K	<a href="#">Weisblum et al., 2020</a>	<a href="https://doi.org/10.7554/eLife.61312">https://doi.org/10.7554/eLife.61312</a>
pCR3.1_GA_S2_K444Q	<a href="#">Weisblum et al., 2020</a>	<a href="https://doi.org/10.7554/eLife.61312">https://doi.org/10.7554/eLife.61312</a>
pCR3.1_GA_S2_K444R	<a href="#">Weisblum et al., 2020</a>	<a href="https://doi.org/10.7554/eLife.61312">https://doi.org/10.7554/eLife.61312</a>
pCR3.1_GA_S2_V445I	<a href="#">Weisblum et al., 2020</a>	<a href="https://doi.org/10.7554/eLife.61312">https://doi.org/10.7554/eLife.61312</a>

(Continued on next page)

**Continued**

REAGENT or RESOURCE	SOURCE	IDENTIFIER
pCR3.1_GA_S2_V445E	Weisblum et al., 2020	<a href="https://doi.org/10.7554/eLife.61312">https://doi.org/10.7554/eLife.61312</a>
pCR3.1_GA_S2_G446S	Weisblum et al., 2020	<a href="https://doi.org/10.7554/eLife.61312">https://doi.org/10.7554/eLife.61312</a>
pCR3.1_GA_S2_G446V	Weisblum et al., 2020	<a href="https://doi.org/10.7554/eLife.61312">https://doi.org/10.7554/eLife.61312</a>
pCR3.1_GA_S2_Y453F	This paper	N/A
pCR3.1_GA_S2_L455R	Weisblum et al., 2020	<a href="https://doi.org/10.7554/eLife.61312">https://doi.org/10.7554/eLife.61312</a>
pCR3.1_GA_S2_L455I	Weisblum et al., 2020	<a href="https://doi.org/10.7554/eLife.61312">https://doi.org/10.7554/eLife.61312</a>
pCR3.1_GA_S2_L455F	Weisblum et al., 2020	<a href="https://doi.org/10.7554/eLife.61312">https://doi.org/10.7554/eLife.61312</a>
pCR3.1_GA_S2_F456V	Weisblum et al., 2020	<a href="https://doi.org/10.7554/eLife.61312">https://doi.org/10.7554/eLife.61312</a>
pCR3.1_GA_S2_Y459F	This paper	N/A
pCR3.1_GA_S2_A475V	Weisblum et al., 2020	<a href="https://doi.org/10.7554/eLife.61312">https://doi.org/10.7554/eLife.61312</a>
pCR3.1_GA_S2_A475D	Weisblum et al., 2020	<a href="https://doi.org/10.7554/eLife.61312">https://doi.org/10.7554/eLife.61312</a>
pCR3.1_GA_S2_G476A	Weisblum et al., 2020	<a href="https://doi.org/10.7554/eLife.61312">https://doi.org/10.7554/eLife.61312</a>
pCR3.1_GA_S2_G476S	Weisblum et al., 2020	<a href="https://doi.org/10.7554/eLife.61312">https://doi.org/10.7554/eLife.61312</a>
pCR3.1_GA_S2_S477G	This paper	N/A
pCR3.1_GA_S2_S477R	This paper	N/A
pCR3.1_GA_S2_T478I	Weisblum et al., 2020	<a href="https://doi.org/10.7554/eLife.61312">https://doi.org/10.7554/eLife.61312</a>
pCR3.1_GA_S2_T478K	This paper	N/A
pCR3.1_GA_S2_V483I	Weisblum et al., 2020	<a href="https://doi.org/10.7554/eLife.61312">https://doi.org/10.7554/eLife.61312</a>
pCR3.1_GA_S2_V483A	Weisblum et al., 2020	<a href="https://doi.org/10.7554/eLife.61312">https://doi.org/10.7554/eLife.61312</a>
pCR3.1_GA_S2_V483F	Weisblum et al., 2020	<a href="https://doi.org/10.7554/eLife.61312">https://doi.org/10.7554/eLife.61312</a>
pCR3.1_GA_S2_E484Q	Weisblum et al., 2020	<a href="https://doi.org/10.7554/eLife.61312">https://doi.org/10.7554/eLife.61312</a>
pCR3.1_GA_S2_E484A	Weisblum et al., 2020	<a href="https://doi.org/10.7554/eLife.61312">https://doi.org/10.7554/eLife.61312</a>
pCR3.1_GA_S2_E484D	Weisblum et al., 2020	<a href="https://doi.org/10.7554/eLife.61312">https://doi.org/10.7554/eLife.61312</a>
pCR3.1_GA_S2_E484G	Gaebler et al., 2021	<a href="https://doi.org/10.1038/s41586-021-03207-w">doi.org/10.1038/s41586-021-03207-w</a>
pCR3.1_GA_S2_G485R	This paper	N/A
pCR3.1_GA_S2_Y489H	This paper	N/A
pCR3.1_GA_S2_F490S	Weisblum et al., 2020	<a href="https://doi.org/10.7554/eLife.61312">https://doi.org/10.7554/eLife.61312</a>
pCR3.1_GA_S2_F490L	Weisblum et al., 2020	<a href="https://doi.org/10.7554/eLife.61312">https://doi.org/10.7554/eLife.61312</a>
pCR3.1_GA_S2_Q493R	Weisblum et al., 2020	<a href="https://doi.org/10.7554/eLife.61312">https://doi.org/10.7554/eLife.61312</a>
pCR3.1_GA_S2_Q493L	Weisblum et al., 2020	<a href="https://doi.org/10.7554/eLife.61312">https://doi.org/10.7554/eLife.61312</a>
pCR3.1_GA_S2_S494L	This paper	N/A
pCR3.1_GA_S2_S494P	Weisblum et al., 2020	<a href="https://doi.org/10.7554/eLife.61312">https://doi.org/10.7554/eLife.61312</a>
pCR3.1_GA_S2_T500I	This paper	N/A
pCR3.1_GA_S2_N501Y	Weisblum et al., 2020	<a href="https://doi.org/10.7554/eLife.61312">https://doi.org/10.7554/eLife.61312</a>
pCR3.1_GA_S2_V503F	Weisblum et al., 2020	<a href="https://doi.org/10.7554/eLife.61312">https://doi.org/10.7554/eLife.61312</a>
pCR3.1_GA_S2_G504D	This paper	N/A
pCR3.1_GA_S2_Y505W	This paper	N/A
pCR3.1_GA_S2_D614G	Wang et al., 2021b	<a href="https://doi.org/10.1038/s41586-021-03324-6">https://doi.org/10.1038/s41586-021-03324-6</a>
pCR3.1 SARS-CoV SΔ19	Schmidt et al., 2020	<a href="https://doi.org/10.1084/jem.20201181">https://doi.org/10.1084/jem.20201181</a>
pCR3.1_pCoV-GX-SΔ19	This paper	N/A
pCR3.1_pCoV-GD-SΔ19	This paper	N/A
pTwist_bCoV-WIV16-SΔ19	This paper	N/A

**Software and algorithms**

GISAID	Elbe and Buckland-Merrett, 2017; Shu and McCauley, 2017	<a href="https://www.gisaid.org/">https://www.gisaid.org/</a> ; RRID: SCR_018251
Prism 8	GraphPad	<a href="https://www.graphpad.com/scientific-software/prism/">https://www.graphpad.com/scientific-software/prism/</a> ; RRID: SCR_002798
Geneious Prime Version 2020.1.2	<a href="https://www.geneious.com/">https://www.geneious.com/</a>	RRID:SCR_010519
Python programming language version 3.7	<a href="https://www.python.org/">https://www.python.org/</a>	RRID:SCR_008394
pandas Version 1.0.5	10.5281/zenodo.3509134	RRID:SCR_018214

(Continued on next page)

### Continued

REAGENT or RESOURCE	SOURCE	IDENTIFIER
numpy Version 1.18.5	10.1038/s41586-020-2649-2	RRID:SCR_008633
matplotlib Version 3.2.2	10.1109/MCSE.2007.55	RRID:SCR_008624
TopHat	10.1038/nprot.2012.016	RRID:SCR_013035
Cufflinks	10.1038/nprot.2012.016	RRID:SCR_014597
ForteBio Analysis software	ForteBio	N/A
QoRTs	10.1186/s12859-015-0670-5	<a href="https://github.com/hartleys/QoRTs">https://github.com/hartleys/QoRTs</a>
htseq-count	10.1093/bioinformatics/btu638	RRID:SCR_011867

## RESOURCE AVAILABILITY

### Lead contact

Requests for further information and or reagents should be addressed to and will be fulfilled by the Lead Contact Paul D. Bieniasz ([pbieniasz@rockefeller.edu](mailto:pbieniasz@rockefeller.edu)).

### Materials availability

All unique/stable reagents generated in this study are available from the Lead Contact following completion of a standard Uniform Biological Materials Transfer Agreement.

### Data and code availability

Coordinates and maps associated with data reported in this manuscript have been deposited in the Electron Microscopy Data Bank (EMDB: <https://www.ebi.ac.uk/pdbe/emdb/>) and Protein Data Bank (PDB: [www.rcsb.org](http://www.rcsb.org)). The coordinates generated from X-ray crystallographic studies of the C032 Fab, C080 Fab, C098 Fab, C099 Fab, C098-RBD complex, and C099-CR3022-RBD complex have been deposited at the PDB with accession numbers 7N3E, 7N3F, 7N3G, 7N3H, 7N3I, and 7R8L, respectively. The coordinates and cryo-EM maps generated from cryo-EM studies of the C032-S 6P complex, C051-S 6P complex, and C548-S 6P complex have been deposited at the PDB and EMDB with accession numbers PDB: 7R8M, 7R8N, 7R8O and EMDB: 24318, 24319, 24320, respectively.

This paper does not report original code.

Any additional information required to reanalyze the data reported in this paper is available from the Lead Contact upon request.

## EXPERIMENTAL MODEL AND SUBJECT DETAILS

### Cell lines

The 293T/ACE2cl.22 (XX) and HT1080/ACE2.cl14 (XY) cell lines were generated in our laboratory ([Schmidt et al., 2020](#); [Weisblum et al., 2020](#)) and were cultivated in DMEM with 10% fetal bovine serum. Cells were periodically examined for mycoplasma contamination and retrovirus contamination by DAPI staining and reverse transcriptase assay, respectively.

## METHOD DETAILS

### Monoclonal antibodies

Antibodies used in this study were described previously and are derived from five different COVID-19 convalescent individuals at 1.3 and 6.2 months ([Gaebler et al., 2021](#); [Robbiani et al., 2020](#)) post infection with SARS-CoV-2. All antibodies were produced using transiently transfected HEK293-6E cells with equal amounts of immunoglobulin heavy and light chain expression vectors. After 7 days, the supernatant was harvested and antibodies were concentrated by ammonium sulfate precipitation and IgG was purified with Protein G-Sepharose 4 Fast Flow ([Robbiani et al., 2020](#)). We expressed 1 antibody per B cell clone, unless a clone was expanded to more than three antibodies at a given time point, in which case we aimed to express at least two antibody sequences. However, this approach failed in the case of C032 where only one antibody was recovered from this clone. Immunoglobulins grouped into the same clonal lineage had their respective IgH and IgL sequences merged and subsequently aligned, using TranslatorX ([Abascal et al., 2010](#)) with the unmutated ancestral sequence obtained from IMG/VT-QUEST reference directory ([Lefranc, 2011](#)). GCTree ([DeWitt et al., 2018](#)) was further used to perform the phylogenetic trees construction. Each node represents a unique IgH and IgL combination and the size of each node is proportional to the number of identical sequences. The numbered nodes represent the unobserved ancestral genotypes between the germline sequence and the sequences on the downstream branch.

### SARS-CoV-2 pseudotyped reporter virus

We used a panel of plasmids expressing RBD mutant SAR-CoV-2 spike proteins in the context of a C-terminally truncated SARS-CoV-2 spike expression plasmid, pSARS-CoV-2-S $\Delta$ 19 ([Weisblum et al., 2020](#)). Additional substitutions to expand the panel were

introduced using synthetic gene fragments (IDT) or overlap extension PCR mediated mutagenesis and Gibson assembly. E484K was originally excluded from our panel because HIV-1-based pseudotypes generated with the E484K substitution in our standard assay were poorly infectious. However, when the E484K substitution was incorporated into a spike protein that also includes that the R683G substitution, which disrupts the furin cleavage site, pseudotyped particle infectivity was preserved. The R683G substitution itself increased pseudovirus sensitivity to some antibodies, including C055, C099, C549 and C512, and antibodies from the C144 and C032 groups. Thus, the E484K, L455R+E484K and KEN (K417N+E484K+N501Y) mutants were used in the context of a pSARS-CoV-2-S  $\Delta$ 19 variant with an inactivated furin cleavage site (R683G). The potencies with which the antibodies neutralized members of the mutant pseudotype panel were compared with potencies against a “wildtype” SARS-CoV-2 (NC\_045512) spike sequence, carrying R683G where appropriate.

Plasmids expressing the spike proteins found in the bat (*Rinolophus Sinicus*) coronavirus BCoV-WIV16 as well as the pangolin (*Manis javanica*) coronaviruses from Guandong, China (pCoV-GD) and Guanxi, China (pCoV-GX) as well as BCoV-RaTG13 were constructed. Spike sequences were codon-modified to maximize homology with the human codon-usage optimized of the pSARS-CoV-2 expressing plasmid VG40589-UT (Sinobiological). The extracellular domain of the bat SARS-like CoV WIV16 (ALK02457.1) is fused to the transmembrane and cytosolic by 19aa truncated domain of SARS-CoV-2-S $\Delta$ 19. It was synthesized by Twist biosciences and provided in a CMV-driven expression vector containing a beta globin intron, named pTwist-BCoV-WIV16-S $\Delta$ 19. The 19aa truncated CDS of BCoV-RaTG13 (QHR63300), PCoV-GD (CoV\_EPI\_ISL\_410721), and PCoV-GX (CoV\_EPI\_ISL\_410542) were synthesized by GeneART and subcloned into pCR3.1 using NheI and XbaI and Gibson assembly, referred to as pCR3.1-BCoV-RaTG13-S $\Delta$ 19, pCR3.1-PCoV-GD-S $\Delta$ 19 and pCR3.1-PCoV-GX-S $\Delta$ 19, respectively.

The SARS-CoV-2 pseudotyped HIV-1 particles were generated by transient transfection (Schmidt et al., 2020). Specifically, virus stocks were harvested 48 h after transfection of 293T cells with pNL4-3 $\Delta$ Env-nanoluc and pSARS-CoV-2 S $\Delta$ 19 and filtered and stored at  $-80^{\circ}\text{C}$ .

### SARS-CoV-2 pseudotype neutralization assays

Monoclonal antibodies were four-fold serially diluted and then incubated with SARS-CoV-2 pseudotyped HIV-1 reporter virus for 1 h at  $37^{\circ}\text{C}$ . The antibody/pseudotyped virus mixture was then added to HT1080/ACE2.cl14 cells. After 48 h, cells were washed with PBS, lysed with Luciferase Cell Culture Lysis reagent (Promega) and Nanoluc Luciferase activity in lysates was measured using the Nano-Glo Luciferase Assay System (Promega) and a Glomax Navigator luminometer (Promega). The relative luminescence units were normalized to those derived from cells infected with SARS-CoV-2 pseudotyped virus in the absence of monoclonal antibodies. The half-maximal inhibitory concentrations for monoclonal antibodies ( $\text{IC}_{50}$ ) were determined using four-parameter nonlinear regression (least-squares regression method without weighting) (GraphPad Prism).

### Selection of antibody resistant rVSV/SARS-CoV-2 variants

To select monoclonal antibody-resistant S variants, rVSV/SARS-CoV-2/GFP<sub>1D7</sub> and rVSV/SARS-CoV-2/GFP<sub>2E1</sub> were passaged to generate diversity, and populations containing  $10^6$  PFU were incubated with monoclonal antibodies (0.5  $\mu\text{g}/\text{ml}$  to 10  $\mu\text{g}/\text{ml}$ ) for 1 h at  $37^{\circ}\text{C}$  before inoculation of  $2 \times 10^5$  293T/ACE2.cl.22 cells in 6-well plates. The following day the medium was replaced with fresh medium containing the same concentrations of antibody. Supernatant from the wells containing the highest concentration of monoclonal antibodies that showed evidence of rVSV/SARS-CoV-2/GFP replication (large numbers of GFP positive cells or GFP positive foci) was harvested 24h later. Where necessary, aliquots (100  $\mu\text{l}$ ) of the cleared supernatant from the first passage (p1) were incubated with the same concentration of monoclonal antibody and then used to infect  $2 \times 10^5$  293T/ACE2.cl.22 cells in 6-well plates, as before (p2). We repeated this process until escape reduced neutralization potency for the antibody was evident, as indicated by increasing numbers of GFP positive cells.

To isolate individual mutant viruses by limiting dilution, the selected rVSV/SARS-CoV-2/GFP<sub>1D7</sub> and rVSV/SARS-CoV-2/GFP<sub>2E1</sub> populations were serially diluted in the absence of monoclonal antibodies and aliquots of each dilution added to individual wells of 96-well plates containing  $1 \times 10^4$  293T/ACE2.cl.22 cells. Individual viral variants were identified by observing single GFP-positive plaques at limiting dilutions. The plaque-purified viruses were expanded, RNA extracted and S sequences determined, and sensitivity to the selecting monoclonal antibody measured.

### rVSV/SARS-CoV-2 neutralization assays

Monoclonal antibodies were five-fold serially diluted and then incubated with rVSV/SARS-CoV-2/GFP<sub>1D7</sub> and rVSV/SARS-CoV-2/GFP<sub>2E1</sub> or plaque purified selected variants for 1 h at  $37^{\circ}\text{C}$ . The antibody/recombinant virus mixture was then added to 293T/ACE2.cl.22 cells. After 16h, cells were harvested, and infected cells were quantified by flow cytometry. The percentage of infected cells was normalized to that derived from cells infected with rVSV/SARS-CoV-2 in the absence of monoclonal antibodies. The half-maximal inhibitory concentrations for monoclonal antibodies ( $\text{IC}_{50}$ ) were determined using four-parameter nonlinear regression (least-squares regression method without weighting) (GraphPad Prism).

### Sequence analyses

To identify putative antibody resistance mutations, RNA was isolated from aliquots of supernatant containing selected viral populations or individual plaque purified variants using NucleoSpin 96 Virus Core Kit (Macherey-Nagel). The purified RNA was subjected to reverse transcription using random hexamer primers and SuperScript VILO cDNA Synthesis Kit (Thermo Fisher Scientific). The cDNA

was amplified using KOD Xtreme Hot Start DNA polymerase (Millipore Sigma) and primers flanking the S encoding sequences. Alternatively, a fragment including the entire S-encoding sequence was amplified using primers targeting VSV-M and VSV-L. The PCR products were gel-purified and sequenced either using Sanger-sequencing or Illumina sequencing (Gaebler et al., 2019). For Illumina sequencing, 1  $\mu$ l of diluted DNA was used with 0.25  $\mu$ l Nextera TDE1 Tagment DNA enzyme (catalog no. 15027865), and 1.25  $\mu$ l TD Tagment DNA buffer (catalog no. 15027866; Illumina). Then, the DNA was ligated to i5/i7 barcoded primers using the Illumina Nextera XT Index Kit v2 and KAPA HiFi HotStart ReadyMix (2X; KAPA Biosystems). Next the DNA was purified using AmPure Beads XP (Agencourt), pooled, sequenced (paired end) using Illumina MiSeq Nano 300 V2 cycle kits (Illumina) at a concentration of 12pM.

For analysis of the Illumina sequencing data, adaptor sequences were removed from the raw reads and low-quality reads (Phred quality score < 20) using BBduk. Filtered reads were mapped to the codon-optimized SARS-CoV-2 S sequence in rVSV/SARS-CoV-2/GFP and mutations were annotated using Geneious Prime (Version 2020.1.2), using a P value cutoff of  $10^{-6}$ . RBD-specific variant frequencies, P values, and read depth were compiled using Python running pandas (1.0.5), numpy (1.18.5), and matplotlib (3.2.2).

### Affinity measurements

Affinity was measured by Biolayer interferometry assays (Wang et al., 2021a). An Octet Red instrument (ForteBio) was used at 30 °C with shaking at 1,000 rpm. The kinetic analysis using protein A biosensor (ForteBio 18-5010) was performed as follows: (1) baseline: 60sec immersion in buffer. (2) loading: 200sec immersion in a solution with IgGs 30  $\mu$ g/ml. (3) baseline: 200sec immersion in buffer. (4) Association: 300sec immersion in solution with WT RBD at 200, 100, 50 or 25  $\mu$ g/ml (5) dissociation: 600sec immersion in buffer. Curve fitting was performed using a fast 1:1 binding model and the Data analysis software (ForteBio). Measurements of anti-SARS-CoV-2 IgGs binding were corrected by subtracting the signal obtained from traces performed with IgGs in the absence of RBD. Mean KD values were determined by averaging all binding curves that matched the theoretical fit with an R2 value  $\geq$  0.8.

### Protein expression and purification

Expression and purification of SARS-CoV-2 6P stabilized S trimers (Hsieh et al., 2020) and SARS-CoV-2 RBD (Cohen et al., 2021) was performed using supernatants of transiently transfected Expi293F cells (GIBCO) and Ni<sup>2+</sup>-NTA affinity and size exclusion chromatography (SEC). Peak fractions from SEC were identified by SDS-PAGE, pooled, and stored at 4 °C. Fabs were generated by papain digestion from purified IgGs using crystallized papain (Sigma-Aldrich) in 50 mM sodium phosphate, 2 mM EDTA, 10 mM L-cysteine, pH 7.4 for 30-60 min at 37 °C at a 1:100 enzyme:IgG ratio. To remove Fc fragments and undigested IgGs, digested products were applied to a 1-mL HiTrap MabSelect SuRe column (GE Healthcare Life Sciences) and the flow-through containing cleaved Fabs was collected. Fabs were further purified by SEC using a Superdex 200 Increase 10/300 column (GE Healthcare Life Sciences) in TBS before concentrating and storing at 4 °C.

### Cryo-EM structure determinations

We incubated purified Fab and S 6P trimer at a 1.1:1 molar ratio per protomer on ice for 30 minutes prior to deposition on a freshly glow-discharged 300 mesh, 1.2/1.3 UltrAuFoil grid or 1.2/1.3 Quantifoil Cu grid. Fluorinated octyl-maltoside was added to the Fab-S complex to a final detergent concentration of 0.02% w/v, resulting in a final complex concentration of 3 mg/ml, immediately before 3  $\mu$ l of complex was applied to the grid. Samples were then vitrified in 100% liquid ethane using a Mark IV Vitrobot after blotting for 3 s with Whatman No. 1 filter paper at 22 °C, 100% humidity.

We followed previously described cryo-EM data collection and processing protocols for Fab-S complexes (Barnes et al., 2020a). Briefly, for all Fab-S complexes, we collected micrographs on a Talos Arctica transmission electron microscope (Thermo Fisher) operating at 200 kV using SerialEM automated data collection software (Mastronarde, 2005). Movies were recorded using a 3x3 beam image shift pattern with a K3 camera (Gatan). Data collection parameters are reported in Table S3. Cryo-EM movies were patch motion corrected for beam-induced motion including dose-weighting within cryoSPARC v2.15 (Punjani et al., 2017) after binning super resolution movies for all datasets. Non-dose-weighted images were used to estimate CTF parameters using a cryoSPARC implementation of the Patch CTF job, and all datasets were processed similarly. Briefly, after picking an initial set of particles based on templates from 2D classification of blob picked particles on a small sub-set of images, this set was pared down through several rounds of 3D classification. *Ab initio* cryoSPARC jobs on a small good subset of these particles revealed distinct states and junk particles. A full set of particles was heterogeneously refined against distinct conformational states and a junk class acting as a trap for bad particles. Particles from each class were separately refined using non-uniform refinement using C1 (C032-S) or C3 symmetry (C051-S and C548-S). Particles from distinct states were re-extracted without binning and were separately refined in rounds of 3D classification. Particles were further subdivided into groups based on beam-tilt and refined separately for CTF parameters and aberration correction. For the C032-S and C051-S datasets, a soft mask (3-pixel extension, 6-pixel soft edge) was generated for the spike S1 subunit and Fab variable domains to improve local resolutions at the Fab-RBD interface. Overall reported resolutions are based on gold standard FSC calculations (Scheres and Chen, 2012).

### Cryo-EM structure modeling and refinement

Initial complex coordinates were generated by docking individual chains from reference structures into cryo-EM densities using UCSF Chimera (Goddard et al., 2018). Models were refined into cryo-EM densities using rigid body and real space refinement with morphing in Phenix (Terwilliger et al., 2018). Models with updated sequences were built manually in Coot (Emsley et al.,

2010) and then refined using iterative rounds of real-space refinement in Phenix and Coot. *N*-Glycans were modeled at potential *N*-linked glycosylation sites (PNGSs) in Coot using 'blurred' maps processed with B-factors generated in cryoSPARC v2.15. We validated model coordinates using MolProbity (Chen et al., 2010; Table S3).

### X-ray structures

To assemble C098-RBD or C099-CR3022-RBD complexes for crystallization, a 3:1 Fab:RBD molar ratio was incubated at RT for 1 h and complexes purified using size exclusion chromatography on a Superdex200 10/300 column (Cytiva) in 1x TBS. Crystallization trials for individual Fabs (C032, C080, C098, and C099), C098-RBD, and C099-CR3022-RBD complexes were carried out at room temperature using the sitting drop vapor diffusion method by mixing equal volumes of the Fab or Fab-RBD complex and reservoir using a TTP LabTech Mosquito robot and commercially available screens (Hampton Research). C032 Fab crystals were grown using 0.2  $\mu$ L of protein complex in TBS and 0.2  $\mu$ L of mother liquor (0.1 M HEPES pH 7.7, 58% 2-Methyl-2,4-pentanediol) and cryoprotected in mother liquor. C080 Fab crystals were grown using 0.2  $\mu$ L of protein complex in TBS and 0.2  $\mu$ L of mother liquor (10% 2-Propanol, 0.1 M BICINE pH 8.5, 30% PEG 1,500) and cryoprotected using Fomblin® oil. C098 Fab crystals were grown using 0.2  $\mu$ L of protein complex in TBS and 0.2  $\mu$ L of mother liquor (2.0 M ammonium sulfate, citric acid pH 3.5) and cryoprotected in mother liquor supplemented with 15% (v/v) glycerol. C099 Fab crystals were grown using 0.2  $\mu$ L of protein complex in TBS and 0.2  $\mu$ L of mother liquor (1.9 M ammonium sulfate, citric acid pH 3.8) and cryoprotected using Al's oil. C098-RBD crystals were grown using 0.2  $\mu$ L of protein complex in TBS and 0.2  $\mu$ L of mother liquor (0.05 M citric acid, 0.05M BIS-TRIS propane pH 5.0, 14% PEG 3,350) and cryoprotected in mother liquor supplemented with 30% (v/v) glycerol. C099-CR3022-RBD crystals were grown using 0.2  $\mu$ L of protein complex in TBS and 0.2  $\mu$ L of mother liquor (0.1M Sodium cacodylate, 40% 2-Methyl-2,4-pentanediol (MPD), and 5% PEG8000) and cryoprotected in mother liquor supplemented with 10% (v/v) glycerol.

X-ray diffraction data were collected for individual Fabs or Fab-RBD complexes at the Stanford Synchrotron Radiation Lightsource (SSRL) beamline 12-2 on a Pilatus 6M pixel detector (Dectris). Data from single crystals were indexed and integrated in XDS (Kabsch, 2010) or iMosflm (Battye et al., 2011) and merged using AIMLESS in CCP4 (Winn et al., 2011; Table S2). Fab structures were solved by molecular replacement using a model of CC12.3 Fab (PDB 6XC4) or HEPC46 Fab (PDB 6MEG). The C098-RBD complex structure was solved by molecular replacement using the C098 Fab (this paper) and RBD (PDB 7BZ5) structures as search models. The C099-CR3022-RBD complex structure was solved by molecular replacement using the C099 Fab (this paper), CR3022 Fabb (PDB 6W41) and RBD (PDB 7BZ5) structures as search models. Heavy chain and light chain CDR loops for the search model Fab were trimmed to make the search models. The structures were refined using an initial round of rigid body and individual B refinement in Phenix (Adams et al., 2010) followed by cycles of manual building in Coot (Emsley et al., 2010) and real space refinement in Phenix with TLS (Table S2).

### Homology modeling of Fab-RBD structures

Homology models for three of the RBD complexes were made for the Fabs of C549 (class 2) for SARS-CoV-2 and C080 (class 3) for both SARS-CoV and SARS-CoV-2. All complexes were modeled based on the cryo-EM structures of the related 1.3 month Fab-S complexes; i.e., the C548-S and C032-S complexes. The Fab of C548 to C549 involved 27 amino acid changes, whereas there were 16 changes for C032 to C080. The RBD of SARS-CoV was modeled upon the C032-S complex. Side chains of residues that were disordered in the density of the experimental structures were also modeled to their correct sequence. Homology models were generated by MODELER (version 9.23) (Sali and Blundell, 1993) and further optimized by Protein Preparation Wizard in Maestro Schrodinger (Sastry et al., 2013) including optimization of hydrogens. The system was fully solvated with SPC water and counter ions. Energy minimization using Brownian Dynamics in Desmond from Schrodinger (version 2020.1) (Bowers et al., 2006) which involved gradually reducing restraints in 100ps steps from the full protein, to the backbone and finally without restraints to avoid any steric clashes.

### Structural analyses

CDR definitions and Kabat numbering for antibody residues were based on IMGT definitions (Lefranc et al., 2015). Figures of structures were made with UCSF ChimeraX. Local resolution maps were calculated using cryoSPARC v 2.15. Areas buried in Fab-RBD interfaces (BSAs) were calculated using PDBePISA (Krissinel and Henrick, 2007) and a 1.4 Å probe. Sc analyses were conducted using Rosetta version 2020.08 (Leaver-Fay et al., 2011). Potential hydrogen bonds were assigned as interactions with A-D-H angle > 90° and between atoms that were < 4.0Å. Potential van der Waals interactions were assigned as interactions that were < 4.0Å. Hydrogen bond and van der Waals interaction assignments are tentative in the cryo-EM structures due to resolution limitations.

### QUANTIFICATION AND STATISTICAL ANALYSIS

The half-maximal inhibitory concentrations for monoclonal antibodies ( $IC_{50}$ ) were determined using four-parameter nonlinear regression (least-squares regression method without weighting) (GraphPad Prism). Numbers of replicates and experiments and statistical tests for each experiment are indicated in the respective figure legends.